An experimental study of basalt–seawater–CO2 interaction at 130 °C

Martin Voigt, Chiara Marieni, Andre Baldermann, Iwona M Galeczka,
Domenik Wolff-Boenisch, Eric H Oelkers, Sigurdur R Gislason

To cite this version:

Martin Voigt, Chiara Marieni, Andre Baldermann, Iwona M Galeczka, Domenik Wolff-Boenisch, et al.. An experimental study of basalt–seawater–CO2 interaction at 130 °C. Geochimica et Cosmochimica Acta, 2021, 308, pp.21-41. 10.1016/j.gca.2021.05.056 . hal-03388372

HAL Id: hal-03388372
https://hal.science/hal-03388372v1

An experimental study of basalt–seawater−CO_2 interaction at 130 °C

Martin Voigt[a,], Chiara Marieni[b], Andre Baldermann[c], Iwona M. Galeczka[a,d], Domenik Wolff-Boenisch[e], Eric H. Oelkers[a,b], Sigurdur R. Gislason[a]*

[a] Institute of Earth Sciences, University of Iceland, Sturlugötu 7, 102 Reykjavík, Iceland (*corresponding author; *e-mail address:* martinvoigt@hi.is)
[b] Géosciences Environnement Toulouse (GET) - CNRS, 14 avenue Édouard Belin, 31400 Toulouse, France
[c] Institute of Applied Geosciences & NAWI Graz Geocenter, Graz University of Technology, Rechbauerstr. 12, 8010 Graz, Austria
[d] GNS Science, Wairakei Research Centre, Taupō 3352, New Zealand
[e] School of Earth and Planetary Sciences, Curtin University, GPO Box U1987, Perth, WA-6845, Australia

Abstract

Over millions of years, the interaction of marine basalt with percolating seawater in low-temperature ocean floor hydrothermal systems leads to the formation of calcite and aragonite. The presence of these minerals in marine basalts provides evidence for substantial CO_2 fixation in these rocks. Here, we report on laboratory experiments to study this process under enhanced CO_2 partial pressures (pCO_2) at 130 °C. Mid-ocean-ridge-basalt (MORB) glass was reacted with North Atlantic Seawater charged with CO_2 in batch experiments lasting up to 7 months. For experiments initiated with seawater charged with ~ 2.5 bar pCO_2, calcite and aragonite are the first carbonate minerals to form, later followed by only aragonite (± siderite and ankerite). For experiments initiated with seawater charged with ~ 16 bar pCO_2, magnesite was the only carbonate mineral observed to form. In total, approximately 20 % of the initial CO_2 in the reactors was mineralized within five months. This carbonation rate is similar to corresponding rates observed in freshwater-basalt-CO_2 interaction experiments and during field experiments of the carbonation of basalts in response to CO_2-charged freshwater injections in SW-Iceland. Our experiments thus suggest that CO_2-charged seawater injected into submarine basalts will lead to rapid CO_2 mineralization. Notably, at pCO_2 of tens of bars, magnesite will form, limiting the formation of Mg-rich clays, which might otherwise compete for the Mg cation and pore-space in the submarine basaltic crust. This suggests that the injection of CO_2-charged seawater into subsurface basalts can be an efficient and effective approach to the long-term safe mineral storage of anthropogenic carbon.

1 Introduction

The urgent need for large scale carbon dioxide removal (CDR) to limit global warming is increasingly evident. It is estimated that between 100 and 1000 Gt of CO_2 will have to be removed from the atmosphere by the end of the 21st century to limit global warming to 1.5 °C compared to pre-industrial levels (Rogelj et al., 2018). Carbon capture and storage (CCS) technologies are an intriguing CDR method as CO_2 can be captured from exhaust streams or directly from the atmosphere. As of 2020, only 40 Mt CO_2 are captured from concentrated sources and stored in geological formations per year (Global CCS Institute, 2020), while global annual CO_2 emissions amounted to 42 Gt CO_2 in 2019 (Friedlingstein et al., 2020). The imbalance between current CCS and anthropogenic CO_2 release highlights the need for research and development of efficient CCS techniques.

Carbon dioxide storage through its mineralization in the subsurface is a low risk technique as carbon bound in stable carbonate minerals has minimal leakage risk (e.g., Matter et al., 2016; Snæbjörnsdóttir et al., 2020). The CarbFix project demonstrated the mineralization of 95% of freshwater-dissolved CO_2 injected into fresh basalts within two years at 20-50 °C and the mineralization of up to 60% of freshwater-dissolved CO_2 injected into altered basalts within several months at 250-270 °C (Matter et al., 2016; Gunnarsson et al., 2018; Clark et al., 2020). A second field project was conducted in the Columbia River Basalt near Wallula (Washington) at 30-45 °C in 2013, where supercritical CO_2 was injected into the subsurface. Hydrological modelling suggests mineralization of up to 60% of the injected CO_2 within two years (McGrail et al., 2017; White et al., 2020).

While the injection method employed in the CarbFix project, i.e. injection of water-dissolved CO_2, drastically reduces the risk of CO_2 leakage to the surface (the injection fluid is not a buoyant fluid), substantial amounts of water are required. At 30 bar pressure and 20 °C, around 22 metric tons of freshwater are needed to dissolve one ton of CO_2 (e.g., Snæbjörnsdóttir et al., 2020). Therefore, the large-scale application of this method requires large amounts of fresh water and faces potential usage conflicts. The use of seawater as a solute is a potential alternative to fresh water. Vast quantities of seawater are available in the immediate vicinity of the basaltic oceanic crust, a reservoir with a storage potential of ~ 3×10^5 Gt CO_2 (Marieni et al., 2013). The capacity of submarine basalts to store vast quantities of CO_2 is supported by the observations of substantial carbonate mineral formation through seawater-basalt interaction. For example, Gillis and Coogan (2011) and Coogan and Gillis (2013) reported that the basaltic oceanic crust can contain ~0.5 to 4.0 wt% of carbonate minerals. These carbonate minerals are formed by the percolation of CO_2-bearing seawater through off-axis hydrothermal systems below the seafloor at temperatures < 100 °C. Moreover, the weathering of marine silicate sediments can result in the formation of as much as ~1 wt% carbonate minerals (Wallmann et al., 2008). While these processes represent an important carbon sink over geological timescales and influence long-term climate regulation (Staudigel et al., 1989; Brady and Gíslason, 1997; Coogan and Gillis, 2013; Isson et al., 2020), only limited data are available on conditions that could enhance and/or accelerate such carbon mineralization processes. Young (< 3 Ma) oceanic crust typically contains only minor amounts of carbonate minerals, suggesting that only limited carbonate precipitation occurs in high temperature mid-ocean ridge hydrothermal systems (Gillis et al., 2001; Heft et al., 2008; Coogan and Gillis, 2018). This is likely related to early uptake of seawater Ca by rapid anhydrite precipitation (Voigt et al., 2018b) and higher stability of non-carbonate Ca and Mg bearing minerals at such conditions. In contrast, carbonate minerals are abundant in the Reykjanes geothermal system, a seawater-dominated on-shore hydrothermal system in southwest Iceland (Wiese et al., 2008; Marks et al., 2010).

Most experimental studies focusing on the chemical reactions during water-basalt-CO_2-interaction have been performed using freshwater (Gysi and Stefánsson, 2012a, b, c; Stockmann et al., 2013, 2014; Galeczka et al., 2013, 2014; Menefee et al., 2017, 2018; Kumar et al., 2017; Clark et al., 2019). Less experimental data are available for seawater systems as shown in Table 1 and described below. A number of experimental studies reacting basalt with seawater under hydrothermal conditions have been published to better understand silicate weathering phenomena and element cycling patterns in mid-ocean ridge systems (e.g., Seyfried, 1977; Bischoff and Seyfried, 1978; Mottl and Holland, 1978; Seyfried and Bischoff, 1979; Mottl et al., 1979; Seyfried and Bischoff, 1981; Seyfried and Mottl, 1982; Voigt et al., 2018b, 2020). However, mineralization of CO_2 was not considered in these studies. Brady and Gislason (1997) found that increasing the $p\mathrm{CO_2}$ in equilibrium with seawater increased basalt dissolution rates slightly, although it remained unclear whether this increase was due to higher dissolved CO_2 concentrations or to a lower liquid phase pH. Wolff-Boenisch et al. (2011) performed a series of far-from-equilibrium basalt dissolution experiments with seawater at 25 °C, and found that the basalt dissolution rates were significantly higher in the presence of seawater compared to freshwater. Similarly, Marieni et al. (2020) measured dissolution rates of submarine basalts and altered gabbro in CO_2-charged seawater, and found that these rates were faster than those measured in freshwater of low dissolved inorganic carbon (DIC) content. Rosenbauer et al. (2012) performed experiments reacting different basalts with CO_2-charged NaCl brines at 50, 100 and 200 °C. The results indicated that 8 to 26% of the available CO_2 was mineralized within ~ 4 months at 100 °C, while lower carbon uptakes were observed at 50 and 200 °C, respectively. The only carbonate mineral product identified in this study was ferroan magnesite (Fe^{II} bearing $MgCO_3$), and the CO_2 uptake correlated with the magnesium content of the rock. In contrast, Shibuya et al. (2013) performed two experiments reacting CO_2-charged aqueous NaCl solutions with basalt. These authors found that the initial 400 mM of dissolved CO_2 was reduced to 0 and 100 mM due to calcite ($CaCO_3$) formation after ~ 3 months, at 250 °C and 350 °C, respectively. In a further study, Luhmann et al. (2017) flooded basalt cores with CO_2-rich NaCl brines. Siderite ($FeCO_3$) formation was suspected based on the calculated liquid saturation states. However, in the three aforementioned studies, no other seawater component (e.g. Mg, Ca, K, …) was introduced to the experiments. The concentrations of such solutes can significantly alter reaction paths. In contrast, Rigopoulos et al. (2017) reacted artificial seawater, initially equilibrated with atmospheric CO_2, with either very fine grained basalt or peridotite at room temperature. In their ~ 2 month long experiments, they detected carbon mineralization in the form of aragonite ($CaCO_3$) only in the peridotite experiments. Finally, Wolff-Boenisch and Galeczka (2018) induced calcite, magnesite, and other Ca/Mg-carbonate precipitation at 90 °C by injecting seawater that was highly supersaturated with respect to carbonate minerals, by the addition of ammonium bicarbonate, into a reactor containing basalt powder.

Although most of these experimental studies demonstrated the potential of using CO_2-charged brines or seawater for carbon mineralization by reacting them with mafic or ultramafic rocks, we are not aware of any experiments that achieved carbon mineralization by reacting CO_2-charged seawater with basalt. To explore and quantify such reactions, a series of batch experiments were run in the present study to mimic the reactions of CO_2-charged seawater injected into a reservoir of basaltic glass at 130 °C. The purpose of the present study is to explore the potential of injecting CO_2-charged seawater into basalt formations for accelerated mineral carbon storage.

2 Methods

2.1 Experimental design

Either natural North Atlantic seawater or synthetic Mg-free seawater (see section 2.2) was reacted with basaltic glass powder and CO_2 in batch experiments at 130 °C. The effects of distinct initial CO_2 partial pressure (pCO_2), water/rock ratio, and the presence or absence of calcite seed crystals were investigated in experiments that ran from 2 to 228 days. All experimental conditions are listed in Table 2. Individual closed system batch experiments were run for each selected sampling duration instead of sampling the liquid repeatedly from single experiments to (1) avoid either CO_2 degassing from the liquid due to an increased headspace after sampling or buffering the solution at low pH if more CO_2 was added to the reactor to maintain pCO_2, (2) obtain a sample of the solids at the same time as obtaining the liquid sample, and (3) maintain a nearly constant water/rock ratio during the experiment.

Three main series of individual experiments were performed to explore the reaction paths and efficiency of carbon mineralization. Most of the experiments were run in the low-pCO_2 series. Experiments in this series are labelled 'Low-#' (where # is the duration in days) in Table 2 and throughout this text. Experiments in this series were started with approximately 2.5 bar pCO_2, resulting in ~ 26 mM DIC in the initial aqueous phase. This DIC concentration is similar to that of the CO_2-charged injection water in the first phase of the CarbFix2 project (Clark et al., 2020). Another experimental series was started with ~ 16 bar pCO_2 in the reactors, resulting in ~ 125 mM DIC in the initial aqueous phase. This is the high-pCO_2 series, and these experiments are labeled 'High-#'. The third experimental series was run using synthetic Mg-free seawater instead of natural seawater and at approximately 2.5 bar pCO_2. This experimental series is referred to as the MgFree series, and these experiments are labeled 'MgFree-#'. Note that some of the individual experiments of the low-pCO_2 series were initiated with different water/rock ratios, lower stirring rates (experiment 'Low-pCO_2-Slow), and in the presence of calcite seeds (experiment 'Low-pCO_2-Calcite') to test the effect of these parameters. A single experiment ('Low-66-146') was sampled once during the experiment to induce degassing of the aqueous phase in the reactor.

An experimental temperature of 130 °C was chosen for this study i) to achieve sufficient reaction progress within reasonable timespans while ii) limiting anhydrite precipitation from the seawater, which occurs at temperatures above ~ 150 °C for standard seawater (Bischoff and Seyfried, 1978) and at lower temperatures for seawater enriched in Ca^{2+} and/or SO_4^{2-}. Such temperature conditions can be found in the margins of coastal geothermal systems such as in Reykjanes, Iceland (e.g. Marks et al., 2010), making the experiments directly applicable to such settings. In addition, batch reactors, as opposed to open systems, were used in this study to achieve sufficient solid reaction products to quantify carbon mineralization when starting directly from CO_2-charged seawater. This is in contrast to many previous carbonation experiments that were initiated at close to neutral or alkaline pH to artificially accelerate the formation of secondary carbonates. Here we allow the initial acidic liquids that are undersaturated with respect to carbonate minerals to evolve towards conditions suitable for carbonation in each individual experiment.

All experiments were conducted in 300 mL or 600 mL Parr titanium reactors as illustrated in Figure 1. The reactor vessels, inner magnetic drive rotors and housings, as well as all parts of the reactor system in contact with liquid during the experiments were made of titanium. All reactors were equipped with Ashcroft G2 500 psig or Omega PX4202 600 psig pressure transducers, type J thermocouples placed in a thermowell, and stirrer tachometers. These sensors were all connected to Parr process controllers and a computer, allowing continuous monitoring of the reactor pressure and temperature, as well as controlling the heating jackets. Pressure readings were converted to absolute pressures by assuming a constant laboratory pressure of 1 atm.

Before starting an experiment, the reactor assemblage was cleaned mechanically and ultrasonically. The reactors were then filled with ~ 0.1 M HCl (where M denotes molality throughout this study, defined as mol per kg water) and heated to the experimental temperature for at least 24 h. The reactors were then emptied, and the same procedure was repeated using ~ 0.1 M HNO_3 and finally with ultrapure H_2O (18.2 MΩ·cm at 25 °C). All reactor assemblages were tested for leaks by filling them with > 20 bar gas and monitoring pressure over at least 48 h.

Experiments were initiated by placing the desired amount of basaltic glass and reactive liquid into the reactor and closing it. The reactor headspace was flushed with pure CO_2 for ~ 30 min by connecting the gas inlet to a CO_2 cylinder and pressure regulator and adjusting reactor pressure to ~ 1.1 bar. The reactor contents were stirred at 600 rpm at room temperature leaving a plug in the reactor head slightly open. Preliminary tests found that this stirring rate was sufficient to maintain the basaltic glass powder in suspension for the employed water/rock ratios. Subsequently, the reactor was closed and heated to the desired experimental temperature within ~ 30 min. Finally, the desired total pressure was set by addition of CO_2 through the gas inlet for ~ 2 h, allowing for CO_2 dissolution into liquid, after which the inlet was closed again, so that the reactors were completely sealed during the experiments.

A single liquid sample was taken from the reactor before ending an experiment. For this, a water-cooled titanium tube with a 0.2 μm cellulose acetate (CA) membrane filter at the end was connected to the sampling outlet. During sampling, a CO_2 cylinder with pressure regulator was connected to the gas inlet again and was set to maintain the same pressure as observed before sampling was initiated. This maintained a constant $p\mathrm{CO}_2$ during sampling. After flushing the outlet with at least 5 mL of liquid, approximately 10 mL of liquid was sampled into a polypropylene (PP) bottle of known mass containing ~ 90 mL of ultrapure water for alkalinity measurements. This immediate 1:10 dilution avoids the possibility of precipitation of solids from the liquid before the analysis. Another 10 mL of liquid was sampled into an acid (HCl) washed PP bottle and acidified with a known amount of Suprapur HNO_3 for analysis by Inductively Coupled Plasma Optical Emission Spectrometry (ICP-OES). An untreated liquid sample of at least 10 mL was taken for fluorine measurements. In several experiments, a 10 mL sample of liquid was collected directly into an Erlenmeyer flask containing a mixture of 5 mL of 5 M NaOH and 5 mL acetone using Norprene tubing for H_2S titrations. Additional liquid samples for redox potential measurements were sampled into a 10 mL PP syringe from some experiments. In experiment Low-66-146, a liquid sample was taken after 66 days to reduce the $p\mathrm{CO}_2$ (and thus increase pH) during the second part of this experiment.

Experiments were stopped by quenching them to room temperature in less than 2 h. The reactor contents were not stirred while cooling to minimize retrograde water-rock interaction. After opening the reactors, the remaining liquid was decanted. The reacted solids were placed in a vacuum filtration system with a 0.2 μm CA membrane filter. The solids were then rinsed a minimum of three times with ultrapure water for ~ 30 to 60 s to remove any remaining experimental liquid. The cleaned solids were dried at room temperature or at temperatures up to 35 °C. Any solids remaining in the reactor (e.g. stuck at the bottom, or precipitated on stirrer shaft, thermowell, or walls) were also collected, cleaned and dried separately.

Thermodynamic calculations were carried out using PHREEQC v3.6.2 (Parkhurst and Appelo, 2013) and the carbfix.dat database v1.1.0 (Voigt et al., 2018a). Quenching simulations were performed to assess the potential for any carbonate mineral precipitation during the cooling of the reactor system (Wolff-Boenisch et al., 2016). In the quenching simulations, the known *in-situ* liquid composition was cooled together with the gas phase contained in the reactor headspace, accounting for pressure changes. Thermodynamic calculations indicate that the liquid was not supersaturated with any carbonate minerals of interest during the quenching procedure (Figure S-1 in the Supplementary Material). Although these calculations predict the supersaturation of the reactor liquid with carbonate minerals after opening the reactors as the $p\mathrm{CO}_2$ decreased to below 1 atm, this is unlikely to have occurred in the few seconds between opening the reactor and decanting the liquid.

2.2 Reactants

The basaltic glass used in this study originated from the Stapafell volcano located within the first fissure swarm of the Reykjanes peninsula where the Mid-Atlantic Ridge comes onshore in SW-Iceland. This basaltic glass is of similar composition as Mid-Ocean-Ridge-Basalt (MORB; Oelkers and Gíslason, 2001; Gíslason and Oelkers, 2003). This material has been extensively characterized and studied (e.g. Wolff-Boenisch et al., 2011; Gysi and Stefánsson, 2012b; Galeczka et al., 2014; Přikryl et al., 2018; Clark et al., 2019). The basaltic glass was ground and sieved to obtain the 45-100 μm size fraction. This size fraction was then ultrasonically cleaned in ultrapure water before it was dried at room temperature. Its chemical composition was determined to be consistent with $\mathrm{SiTi_{0.02}Fe^{2+}_{0.17}Fe^{3+}_{0.02}Mg_{0.28}Ca_{0.26}Na_{0.08}K_{0.008}O_{3.45}}$ by Oelkers and Gislason (2001), and its specific surface area was measured by Clark et al. (2019) using the BET technique (Brunauer et al., 1938) and determined to be 1240 $\mathrm{cm^2/g}$. Powdered basaltic glass (> 90 wt.% glass; < 10 wt.% forsterite) was used instead of larger pieces to increase the chemical reactivity so that sufficient reaction progress is achieved during the experiments.

Most experiments were started using natural seawater collected from the Faxaflói 9 station, located offshore west of Iceland (64° 20’ N, 27° 58’ W), at 3 m depth during February 2011 (Jones et al., 2012). The seawater was filtered and acidified using HCl upon collection and stored in the dark at < 10 °C. Prior to each experiment, sufficient aqueous 1 M NaOH solution was added to an aliquot of this seawater so that its alkalinity was ~ 2.3 meq/kg (Table 2), corresponding to that of standard seawater (Millero et al., 2008). Other experiments used synthetic Mg-free seawater, prepared by weighing reagent grade NaCl, $\mathrm{Na_2SO_4}$, $\mathrm{CaCl_2{\cdot}2H_2O}$, KCl, $\mathrm{NaHCO_3}$, $\mathrm{Na_2CO_3}$ and NaF into a container with ultrapure water, followed by thorough mixing and storage at < 10 °C in the dark until use. Similar to the natural seawater, a final adjustment of the alkalinity to ~ 2.3 meq/kg was done by adding small amounts of a 1 M NaOH solution.

2.3 Analysis of liquids

Alkalinity titrations of liquid samples were carried out with an aqueous ~ 0.001 M HCl solution and a Cole Parmer double junction glass pH electrode using the Gran (1952) method. Alkalinity titrations were performed in duplicate. The 95% confidence interval, used for stated uncertainties throughout this text, was determined to be approximately ± 0.5 % based on repeated measurements.

The concentrations of Na, Ca, S, Mg, Cl, Fe, K, Al, and Si in all liquid samples were determined using a Spectro Ciros Vision ICP-OES. All measurements were carried out in duplicate on samples diluted 10-, 100-, and 1000-fold in an aqueous 1% $\mathrm{HNO_3}$ solution. Uncertainties were estimated from repeated measurements to be approximately ± 3 % for major elements. Detection limits were ~ 4 μM for Al, ~ 1 μM for Fe, and ~ 20 μM for Si. The concentrations of all other elements were above detection limits for all samples. Fluorine concentrations were determined using a F^- selective electrode, and corrections were made for the presence of aqueous MgF^+ complexes based on the procedure described in Kleine et al. (2020).

The pH and DIC values at experimental temperatures were calculated using measured alkalinities, the elemental composition of the liquid, and the pressure recorded by the pressure transducers mounted on the reactors via thermodynamic calculations. This approach makes use of the fact that the total pressure in the reactor is determined by the equilibrium of H_2O and CO_2 between the liquid and gas phases. The pH and DIC calculated for the experimental temperature are estimated to have an uncertainty of approximately 0.07 pH units and 3 mM, respectively, based on propagating uncertainties using Monte Carlo methods (e.g. Anderson, 1976). For this, the uncertainty of pressure measured using the transducer was assumed to be 0.1 bar. In some cases, the pH of a liquid aliquot sampled from the reactor at shut-down was measured using a Thermo Fisher Scientific Eutech double junction plastic combination pH electrode. Although these measurements are affected by degassing of the liquid, their values are similar to those calculated using the measured total pressure when corrected to the experimental temperature using thermodynamic calculations. Some comparisons of measured and calculated pH values are provided in Figure S-2 in the Supplementary Material.

Samples for total sulfide sulfur (S^{II-}) concentration measurement were first taken up in aqueous NaOH and acetone solutions. The resulting liquid was then passed through filter paper to remove precipitates formed due to the pH increase of the seawater. The recovered liquids were then titrated with an aqueous $(CH_3COO)_2Hg$ solution using dithizone as indicator as described by Arnórsson et al. (2006). The detection limit of these measurements was approximately 1 μM S^{II-}.

A Microelectrodes MI-800 Ag-AgCl Micro Combination Redox Electrode was used for redox potential measurements at ambient temperature and pressure conditions. Measurements were converted to the standard H_2 electrode reference state using the equations of Wolkersdorfer (2008) for the specific electrode type. The redox potential at *in situ* pressure and temperature conditions were then calculated using the same thermodynamic data as in other calculations.

2.4 Analysis of solids

The basalt powder used as reactant and the solid reaction products collected at the end of each experiment were analyzed using a Zeiss Leo Supra 25 Scanning Electron Microscope (SEM) equipped with an energy-dispersive spectrometer (EDS) located at the Innovation Center Iceland. Samples were gold-coated and analyzed using an acceleration voltage of 20 kV, an aperture of 30 μm, and a working distance of 8.5 mm.

Total inorganic carbon (TIC) contents of the solids were determined using a system originally designed for DIC analysis located at the GET Laboratory, Toulouse, France (Bénézeth et al., 2011). This system uses a non-dispersive infrared (NDIR) CO_2 gas analyzer to measure the mass of CO_2 released from a sample upon addition of a 1 M aqueous HCl solution. A CO_2-free carrier gas transports the released gas phase to the NDIR detector. The detection limit is approximately 0.0005 wt% CO_2, and the relative uncertainty of measurements was ~ 6 %, as determined by repeated measurements. Note that sample heterogeneity likely contributes significantly to this value. Measurement of the TIC content of solids collected from the high-pCO_2 experiment was not possible using this method, as the dissolution of the magnesite present in these samples is slow even in concentrated acids. TIC was also measured by heating the solids to 1000 °C in a furnace in a pure nitrogen environment and detecting the released carbon with a solid-state infrared cell using an ELTRA CW-800 at Activation Laboratories Ltd., Canada. This latter method has a higher detection limit of 0.01 wt% CO_2 and higher relative uncertainties equal to 100% at the detection limit, which decreases to 20% at 0.1 wt% CO_2 in a sample. Nevertheless, this approach allowed the determination of the CO_2 contents of the samples containing magnesite.

X-ray diffractometry (XRD) measurements were carried out to characterize the identity of alteration minerals in reacted samples using a PANalytical X'Pert PRO diffractometer fitted with a Co-sourced X-ray tube (40 kV, 40 mA) and a high-speed Scientific X'Celerator detector. The solids were analyzed without grinding and applying the top-loading technique to allow the identification of trace amounts of secondary carbonates. This approach enhances the intensities of carbonate-diagnostic reflections due to crystal size effects (Baldermann et al., 2020). The solids were examined between 4 and 85 °2ϴ with a step size of 0.008 °2ϴ and a count time of 40 s per step. The recorded XRD patterns were analyzed by the PANalytical Highscore Plus software suite (version 3.0.4) and its pdf-4 database (Baldermann et al., 2018).

3 Results

3.1 Evolution of liquid compositions

The composition of all collected liquid samples is provided in Table 3 and shown as a function of experiment duration in Figure 2. The *in situ* pH increased rapidly during the experiments, from ~ 5.1 in the low-pCO_2 experiments or ~ 4.3 in the high-pCO_2 experiments to ~ 5.6 and 5.0, respectively. The pH in the experimental liquids remained relatively stable at these levels after the initial increase. Alkalinity increased in the liquids of all experiments from an initial ~ 2.3 meq/kg. Within the first two hours, while the experiments were charged and equilibrated with CO_2 before disconnecting the reactor from the CO_2 source, alkalinity rose to ~ 7.3 meq/kg. The highest alkalinities were recorded in experiments of < 100 days and those in the high-pCO_2 series, where 9.4 meq/kg was reached. Calculated DIC concentrations at the beginning of the experiments, after charging the reactors with CO_2, were ~ 26 mM in the low-pCO_2 experiments and ~ 125 mM in the high-pCO_2 experiments. These values decreased to a minimum of 12 mM and 105 mM, respectively, during these experiments.

During the low-pCO_2 experiments, the Mg concentrations of the reactive liquids significantly decreased from an initial 54 mM to a minimum of 16 mM, while Ca concentrations gradually increased from 10 mM to 31 mM. Silica and Fe concentrations increased rapidly from below the detection limit to ~ 4 mM and 0.06 mM, respectively, and stayed relatively constant afterwards. Sulfate sulfur (S^{VI}) decreased over time in the experiments, from 29 mM down to a minimum of 7 mM. Sulfide sulfur (S^{II-}) was only analyzed in longer duration experiments and its concentrations were above the detection limit only in experiment 'Low-pCO_2-Slow', where 9.5 µM was measured. Fluoride concentrations increased significantly from the initial 40 µM to 277 µM after 5 days, but were systematically lower in the longer duration experiments with a minimum of 8 µM. Similarly, Al concentrations increased initially to 8 µM, but were at or below the detection limit of ~ 1 µM in the samples collected at the end of the longer duration experiments.

During the high-pCO_2 experiments, the liquid composition evolved in a similar direction as in the low-pCO_2 experiments, although the magnitude differed. Magnesium decreased only to 46 mM and Ca increased to 12 mM. On the other hand, Si and Fe increased to a greater extent in the high-pCO_2 experiments compared to the low-pCO_2 experiments, to 6.6 mM and 0.19 mM, respectively. Sulfate sulfur decreased slightly less, to 16 mM, and Al and F evolutions are similar to the trends seen in the low-pCO_2 experiments.

In the experiments conducted with synthetic Mg-free seawater, the opposite trends were observed for some elements. Magnesium in the liquid increased from below detection limit to 5 mM, while Ca concentrations decreased initially to 4 mM before increasing again to 8 mM after 150 days. Furthermore, S^{VI} decreased less strongly in these experiments, to a minimum of 23 mM. The liquids collected from the longest duration experiment in this series had a F concentration of 897 µM, and an Al concentration of 11 µM, which is significantly higher than in the other experiments. On the other hand, Si and Fe show similar increases in this series compared to other experiments.

The highest Ca concentration was measured in experiment 'Low-pCO_2-Calcite', which was started in the presence of 102 mg of calcite seeds, corresponding to ~ 0.1 wt% of the total solid mass. These seeds were added to accelerate the initial pH increase and alkalinity generation and to assess the effect of the presence of small quantities on carbonation rates. The presence of these seeds added up to 4.7 mM of Ca and 9.5 meq/kg of alkalinity to the liquid. Similar effects potentially occur in natural systems where calcite is present in the host rocks. For example, the basaltic oceanic crust can contain ~0.5 to 4.0 wt% carbonates (Gillis and Coogan, 2011; Coogan and Gillis, 2013), and initial calcite dissolution likely occurred during CO_2-charged freshwater injection into basaltic rocks in Iceland (Snæbjörnsdóttir et al., 2017).

Liquid K, Na, and Cl concentrations remained close to constant throughout the experiments as shown in Table 3 and the Figure S-3 in the Supplementary Material. Nevertheless, the strong positive correlation between the Na and Cl concentrations of the reacted seawater, with a Pearson r value of 0.89, suggests some water evaporation during the experiments. As the gas in the reactor headspace contained relatively little water vapor, this evaporated water was most likely present in condensed form in the inner magnetic drive rotors and other accessories of the upper reactor assemblage, and/or evaporated during the initial flushing of the reactor with CO_2 (see section 2.1). Significant loss of H_2O from the reactor system is unlikely to have occurred because: (1) No significant correlation was found between the experiment duration and Na or Cl concentrations, (2) the loss of water vapor would have been accompanied by a CO_2 loss of a similar magnitude, and (3) all reactors were tested for leaks by pressurizing them to a pressure significantly above those used during the experiments.

The redox potential of the sampled liquids decreased from the initially oxidizing conditions (pE ~ 4 to 5) to moderately reducing pE of around zero. This redox potential evolution is shown in Figure 3. Assuming thermodynamic equilibrium of the redox couples, these redox potentials indicate that practically all the aqueous iron is present as Fe^{II} (Figure 3). This dominance of Fe^{II} suggests that the relatively small amounts of Fe^{III} released from the basaltic glass were taken up by secondary phases such as clays and hematite (see below). At this pE, practically no H_2S is expected to be present in the reactor, which agrees with the measured H_2S concentrations, which were mostly below the detection limit (Table 3). It is unclear, however, if redox equilibrium was achieved during the experiments as they were run at 130 °C (e.g., Stumm and Morgan, 1996; Kaasalainen and Stefánsson, 2011). This prevents a more detailed interpretation of these measurements.

3.2 Solid reaction products

The solids recovered from the reactors at the end of the experiments were markedly altered. The bulk of the solids were found to be present as loose powder after the experiments.

SEM images, in conjunction with EDS and XRD analyses, revealed that significant amounts of the initially smooth and clean basaltic glass grain surfaces of the basalt were covered with a honeycomb-shaped layer of saponite, a trioctahedral smectite rich in Mg (Figure 4 A, C, D, Figure 5). The identity of these clays was verified by XRD as ferrous saponite, as indicated by broad and asymmetric reflections at ~15 Å (d_{001}), 6.1 Å (d_{002}), 4.5 Å (d_{020}), 3.2 Å (d_{004}), 2.6 Å ($d_{13,20}$), 1.7 Å ($d_{15,24,31}$) and 1.53 (d_{060}) Å (Decarreau et al., 2008; Baldermann et al., 2014). In some cases, the initial stages of smectite growth could be seen (Figure 4 D), and some basaltic glass grains almost completely covered by smectite were also found. In places the underlying glass surfaces could be seen beneath the smectite precipitate (Figure 4 C). Furthermore, rounded grains suggest significant dissolution of the initial basaltic glass (Figure 4 B). Anhydrite appears as elongated or platy particle shapes attached to existing basalt grains (Figure 4 E). Based on EDS spectra and the evidence from XRD (see below), precipitates with a pseudohexagonal form, twinning (c.f. Sand et al., 2012) and Ca, C and O composition were identified as aragonite (cf. Figure 4 F, from the experiment 'Low-66-146').

In addition to the minerals identified by SEM, XRD patterns of the retrieved powders indicate the presence of small amounts of aragonite in the solids recovered from most of the long-term experiments. Calcite was identified in the solids collected in experiments 'Low-44', 'Low-57', and siderite in experiments 'Low-148' and 'Low-pCO$_2$-Slow'. Ankerite was identified in the solids collected from experiment 'Low-148'. Magnesite was identified in the solids collected after the longer high-pCO$_2$ experiment 'High-140' (see Figure 5 and the Figure S-6 in the Supplementary Material). Furthermore, XRD data show that zeolites and hematite were present in small amounts in the solids collected from some experiments. The only primary crystalline mineral phase detected by XRD was forsterite (in both the initial basalt as well as the reacted samples), while the majority of all samples is the basaltic glass starting material.

In some cases, material was found to be stuck to the reactor bottom in the form of a cone. This is likely due to the slower fluid dynamics below the stirrer. This was most pronounced in the experiment 'Low-pCO$_2$-Slow', where stirring was reduced to 20 rpm for most of the experiment. No other correlations between the presence of powder stuck to the reactor bottom and experimental parameters were found. Furthermore, minor amounts of light-colored precipitates were found on reactor walls, thermowells, sampling dip-tubes and stirrer shafts. EDS spectra and XRD patterns suggest that these solids are mainly comprised of anhydrite and smectite.

3.3 Carbon content of the solids and carbon mass balance

The TIC present in the reacted solids measured by both methods described above are presented in Table 4 and Figure 6. These results show significant carbon uptake by the solids during the experiments. The agreement between both analytical methods is good, but the significant uncertainties of the furnace method at low CO_2 contents, as well as its higher detection limit, lead to small differences for some experiments. A further approach to estimating the amount of carbon mineralized during the experiments is via the determination of carbon remaining in the fluid phases at the end of each experiment. The total amount of carbon present in the reactor fluids (liquid and gas) can be estimated using thermodynamic principles from the temperature, total pressure, volumes of the respective phases, and the composition of the liquid including its alkalinity. This mass balance relation can be expressed as

$$n_{\mathrm{CO_2}}^{\mathrm{Fluids}} = n_{\mathrm{CO_2}}^{\mathrm{Liquid}} + n_{\mathrm{CO_2}}^{\mathrm{Gas}} = \mathrm{DIC} \cdot m^{\mathrm{Liquid}} + \frac{p_{\mathrm{CO_2}}}{P} \cdot \frac{V^{\mathrm{Gas}}}{V_m}$$

where $n_{\mathrm{CO}_2}^{x}$ stands for the molar amount of CO_2 in x, m^{Liquid} refers to the mass of liquid, P desginates the total pressure, and V^{Gas} and V_m denote the volume of the headspace and the molar volume of the gas, respectively. Similar to other thermodynamic calculations in this study, p_{CO_2} and V_m were calculated using PHREEQC. The difference between the carbon calculated to be in the fluid phases at the beginning and end of the experiments equals that mineralized during the experiments. These results of this calculation are provided in Table 4.

All methods used to determine the mass of carbon incorporated into the solids during the experiments show a trend of increasing CO_2 mineralization with experiment duration. In the low-pCO_2 series, around 19% of the total mass of carbon present in the reactor was mineralized after 150 days. In comparison, the Mg-free experimental series exhibits ~ 33% mineralization after 150 days (experiment MgFree-150). The solids recovered from both high-pCO_2 experiments exhibited slow CO_2 release during acidification-TIC measurements indicating the presence of magnesite. Furnace-TIC measurements indicate ~ 14% of the CO_2 mineralized after 140 days in the high-pCO_2 experimental series. This is slightly less than that over this time frame during the low-pCO_2 experiments. However, the absolute amount of CO_2 mineralized in the high-pCO_2 experiments is significantly higher due to the higher mass of CO_2 introduced into the reactor at the beginning of these experiments. Expressed as CO_2 wt% in the solids, the longest duration high-pCO_2 experiment had 0.37 wt% CO_2 in the recovered solids while the longest duration low-pCO_2 experiment had only ~ 0.11 wt% CO_2 in the recovered solids.

The highest mineralization of 55 ± 9 % CO_2 was measured in the experiment 'Low-pCO_2-Calcite' which was ran with calcite seeds. The calcite seeds rapidly dissolved under the acidic conditions prevailing at the beginning of the experiments, increasing the liquid pH, Ca concentration, and alkalinity. XRD or SEM analysis indicates the initial calcite seed crystals were completely dissolved during the experiments. A similar high carbon mineralization (53 ± 4% CO_2) is suggested by mass balance calculations for the 'Low-pCO_2-Slow' experiment. While the three methods for measuring carbon mineralization generally show a relatively good agreement with each other, differences exist. A notable example is the experiment MgFree-140, where mass balance calculations suggest minor CO_2 mineralization, while both methods for quantification of carbonates in the solids revealed a higher CO_2 mineralization. The reason for these differences is unclear.

4 Discussion

4.1 General trends of seawater-basalt-CO_2 interaction

As evident in Figure 2, basalt dissolution causes a rapid initial increase in alkalinity and pH in all experiments. Subsequently, the pH is buffered by a balance between basalt dissolution and secondary mineral precipitation as well as by the presence of bicarbonate. Otherwise, the evolution of the aqueous chemistry differs among the experimental series due to distinct secondary mineral formation behaviour. In the low-pCO_2 series, substantial smectite clay precipitation, as seen in XRD and SEM observations (Figure 4 and Figure 5), leads to a strong decrease in aqueous Mg concentrations and low aqueous Fe concentrations. At higher pCO_2, smectite clay precipitation is significantly less pronounced, as suggested by the smaller decrease in aqueous Mg concentrations and higher Fe concentrations. As aqueous Al concentrations remain low in both of these experimental series, it is likely that a poorly crystalline aluminosilicate phase such as allophane or amorphous Al-hydroxides formed consuming aqueous Al. In many experiments, aqueous Al concentrations were below the detection limit of ~ 1 µM, allowing only the calculation of maximum saturation indices (SI) for relevant aluminosilicates (Figure S-4 in the Supplementary Material). Nevertheless, allophane was potentially at saturation, and Mg-saponite was potentially significantly oversaturated, but less so in the high-*p*CO_2 series, in agreement with the trends described above. Thermodynamic calculations also suggest that chalcedony is slightly oversaturated in the sampled liquids (Figure 7), indicating that this phase potentially formed even though it was not detected by XRD. This may be due to the fine-grained nature of this phase (Gíslason et al., 1997). In both experimental series run in natural seawater, basalt dissolution releases Ca to the liquid, eventually leading to anhydrite precipitation. This results in a decrease in aqueous S^{VI} concentrations. The rapid anhydrite precipitation is further evidenced by the saturation indices at the end of the experiments, which were close to equilibrium with respect to anhydrite (see Figure 7). Although Fe is mostly released from the basalt in reduced form, the reduction of S^{VI} to S^{II-} appears to be negligible (Table 3), preventing Fe-sulfide mineral precipitation. Furthermore, the aqueous solutions became supersaturated with respect to different carbonate minerals due to increases in pH, alkalinity, and aqueous Ca (and Fe) concentrations (Figure 7). This leads to carbonate mineral precipitation, which is discussed in detail in the following sections.

Experiments run in the presence of Mg-free seawater exhibit several differences compared to those run in natural seawater. While the pH is buffered at similar or slightly higher values compared to natural seawater, no strong decrease in alkalinity was observed. The lack of Mg in the liquid leads to the formation of zeolite minerals instead of smectite clays as seen in the XRD data (Figure 5). The formation of zeolite minerals consumes aqueous Ca. The high aqueous Al concentration measured in liquids of this series after 150 days is likely a consequence of the formation of Al-F aqueous complexes due to elevated aqueous F concentrations (Tagirov and Schott, 2001).

4.2 Reaction path simulations

Reaction path calculations were performed to estimate the mass of secondary minerals precipitated during the individual experiments. This was not possible to determine directly from the experiments due to the large number of reacting phases and their variable composition. The reaction path models were calibrated against the first 150 days of data from each experimental series. The calibrations took account of the observed identity of secondary phases, the liquid compositions, and the amount of CO_2 mineralized in the three experimental series: low-*p*CO_2, high-*p*CO_2, and Mg-free. While two experiments were run for 204 and 228 days (experiments Low-*p*CO_2-Slow and Low-*p*CO_2-Calcite), both of these represent special conditions. One was run at slow stirring rates, and one contained 102 mg calcite seeds to accelerate initial reactions. As it is unclear how much influence these conditions had on the reaction progress, they were not included in the calibration of the reaction path calculations.

The secondary phases considered in the models were restricted to those observed by SEM and XRD analysis, notably Mg-Mg and Mg-Fe saponite, anhydrite, hematite, Ca-stilbite, aragonite or magnesite for low- and high-*p*CO_2, respectively. Chalcedony and allophane were included as well, although these phases are not detectable by XRD. The total amount of basaltic glass dissolved was adjusted to fit the observed liquid compositions for the reaction progress during the ~ 5 month experiments. A slight adjustment of the solubilities of some phases was made to improve the fit of the measured liquid compositions. A list of the revised equilibrium constants is provided in Table S-1 in the Supplementary Material. These adjustments of mineral solubility are within the uncertainties associated with the thermodynamic data under such conditions (e.g., Voigt et al., 2018a). Furthermore, the equilibrium constants for secondary aluminosilicate precipitation reactions had to be increased substantially compared to those of the Voigt et al. (2018a) database to reproduce the observed liquid composition trends of the experiments (see Table S-1 in the Supplementary Material). This is most likely due to the sluggish precipitation kinetics of these minerals compared to the other secondary phases. Without these equilibrium constant changes, these aluminosilicates are predicted to rapidly consume most of the alkalinity generated by the basaltic glass dissolution, impeding carbonate mineral precipitation. This observation highlights the importance of slow aluminosilicate precipitation vs faster carbonate mineral precipitation for carbon mineralization. Note that it is unclear if aluminosilicate precipitation would become dominant over timescales beyond those of our experiments, as proposed by Rigopoulos et al. (2017). It was not possible to accurately reproduce the observed experimental trends assuming secondary phases precipitated at local equilibrium together with a laboratory-measured basaltic glass dissolution rate equation. This suggests that secondary silicate mineral precipitation is the overall rate determining process of the coupled basalt dissolution/carbonate precipitation process. Note that secondary aluminosilicate precipitation removes substantial Si and Al from the liquid and lowers the pH, which both cause the reactive liquid to remain strongly undersaturated with respect to hydrated basaltic glass, promoting its dissolution. This is consistent with the observation that doubling the amount of basalt in the reactor, i.e. a reduction of the water/rock (W/R) ratio, did not significantly increase the amount of CO_2 mineralization (Figure 6). This indicates that the reactive surface area of the basalt is not directly correlated to the degree of CO_2 mineralization observed in our experimental series.

To compare and calibrate the results of the reaction path models to the experiments, reaction time was calculated as a linear function of dissolved basaltic glass. To achieve a good fit to the experimental data, between 40% to 80% faster dissolution was assigned to the first 50 days of the models compared to the subsequent days. This model approach reflects the natural environment in so far that secondary clay precipitation on altered basalt surfaces potentially slows dissolution. After such adjustments, the resulting calculated liquid concentrations and carbonation rates reproduce the observed experimental trends relatively well (see Figure S-5 in the Supplementary Material). Nevertheless, some differences exist, such as a poor estimation of pH and thus also alkalinity in the low-pCO$_2$ simulation.

The results of the calculations, as shown in Figure 8, suggest that different amounts of basaltic glass dissolution were required to achieve the experimentally observed liquid compositions and mass of CO_2 mineralization after 5 months. Specifically, the dissolution of 12.5 g of basalt per kg of water was required to reproduce the observations of the low-pCO$_2$ experiments, 6.7 g of basaltic glass dissolution was required per kg of water to reproduce the observations of the high-pCO$_2$ experiments, and 3.3 g of basaltic glass dissolution was required per kg of water to reproduce the observations of the Mg-free seawater experiments. These differences may stem from the significantly larger amount of saponite precipitation in the low-pCO$_2$ experiments; saponite precipitation removes Si and Al from the liquid promoting further basaltic glass dissolution. The only (alumino)silicate minerals predicted to form in significant amounts during the high-pCO$_2$ experiments are allophane and chalcedony. The only (alumino)silicate mineral predicted to form in significant amounts during the Mg-free experiments is Ca-stilbite (see Figure 8). Such computed results are consistent with observations from the solids recovered after the experiments. Small amounts of anhydrite formation are predicted in all experimental systems due to the release of Ca from the basaltic glass. Rapid early anhydrite formation is only predicted to occur from basaltic glass interaction with the synthetic Mg-free seawater at 130 °C due to the lack of aqueous Mg-SO_4 complexation; this complex increases anhydrite solubility in natural seawater.

The reaction path models give new insights into the mineralogical and chemical differences of the solids and liquids observed among the different experiment series. The lack of saponite precipitation from the synthetic Mg-free seawater experiments leads to higher alkalinity and thus a higher degree of carbon mineralization during the experiments (Figure 8). As saponite formation is also largely suppressed in the high-pCO_2 experiments, and aqueous Mg is consumed by magnesite precipitation, as seen in the experiments, the absolute amount of CO_2 mineralization is significantly higher under these conditions. At the same time, however, the degree of CO_2 mineralization during the high-pCO_2 experiments is comparable to the low-pCO_2 series, as significantly more CO_2 was introduced into the system in the former.

4.3 Identity of carbonate minerals

The predominant carbonate mineral identified in the reacted solids of most experiments was aragonite, with some experiments also producing calcite, siderite, ankerite, and magnesite (Figure 5). The predominance of aragonite over calcite as $CaCO_3$ polymorph is in agreement with studies of young (< 15 Ma) marine sediments and hydrothermal crustal aquifers showing the widespread presence of aragonite (Coogan and Gillis, 2018). Older marine carbonates are dominated by calcite. This is interpreted to be caused by a lower Mg/Ca concentration ratio of seawater during the time of mineral formation (Morse et al., 1997; Stanley and Hardie, 1998, 1999). No such correlation could be found in our experiments, as aragonite was formed in experiments performed in either natural seawater or synthetic Mg-free seawater. Calcite was observed only from the solids recovered from the relatively short duration experiments, while aragonite was predominant in longer experiments. This observation is potentially due to slightly higher initial supersaturation of the liquid with respect to calcite during the shorter experiments (Figure 7), although this could also be affected by the precipitation kinetics of these two minerals. The results of this study contrast with that of Shibuya et al. (2013), who reacted a CO_2-charged NaCl brine with basalt at 250 °C and 350 °C and an initial DIC of 400 mM. The carbonate mineral formed during these experiments was calcite even after ~ 3 months of experiment. It is unclear if the difference between the results of the Shibuya et al. (2013) experiment and those of the present study is due to their higher temperature, higher initial DIC, or different initial reactive solution composition. Similarly, calcite was the only authigenic carbonate mineral found in drill cores recovered from the Surtsey geothermal system, a seawater-dominated and basalt with fluid temperatures of 40-141 °C (Kleine et al., 2020). As Mg and Ca concentrations observed in this system are similar to those in our experiments, the reason for this difference is unclear. Calcite is also the only carbonate mineral found in the Reykjanes system, where fluids close to seawater composition circulate through a basaltic hydrothermal system (Wiese et al., 2008; Marks et al., 2010). The fact that the fluids in the Reykjanes system are heated and undergo fluid-rock interaction at temperatures of ~ 260 to 310 °C, much higher than in our experiments, make the identification of the reason for this difference difficult. Potential reasons for the difference in carbonate mineralogy between this natural system and our experiments include i) the depletion of the fluids in Mg or other elements due to fluid-rock interaction before carbonate precipitation occurred, and ii) the presence of minerals such as illite, chlorite, epidote, garnet, and pyrite in the system (Marks et al., 2010).

Thermodynamic calculations indicate that the final reactive liquids in all of our experiments were close to or supersaturated with respect to aragonite, ankerite, and siderite (Figure 7), while the initial CO_2-charged seawater was undersaturated with respect to these minerals. This change is mainly due to the increase in pH, associated with changes in the speciation of DIC. Similar saturation index evolutions are observed for calcite, magnesite, and dolomite. The absence of the latter two minerals from the solids recovered from all experiments other than those performed at high-pCO_2 could stem from kinetic inhibition. Magnesite precipitation was only observed in the higher pCO_2 experiments performed in this study. It is unclear whether this observation stems from the higher DIC, lower pH, and/or the lower amount of smectite precipitation of these experiments. As smectite precipitation reduces dissolved Mg concentrations in natural marine hydrothermal fluids at temperatures above ~ 60 °C (Coogan and Gillis, 2018), the low amount of smectite formed in our experiments is likely a key for magnesite formation. This conclusion is consistent with that of Rosenbauer et al. (2012), who observed ferroan magnesite formation during the reaction between a CO_2-charged NaCl brine with basalt at ≥ 1 M DIC and temperatures from 100 to 200 °C.

No correlation between the observation of siderite/ankerite in some solids and experimental conditions or liquid compositions is evident, as these two carbonate minerals only precipitated during two experiments. Thermodynamic calculations indicate that the experimental liquids showed the highest supersaturation with respect to dolomite, and, in descending order, ankerite, magnesite, siderite, calcite, and aragonite. The fact that the most abundant mineral found in the experimental solids is aragonite, and magnesite for the high-pCO_2 experiments, highlights the importance of factors other than thermodynamics influencing the identity of precipitating carbonate minerals.

4.4 Comparison to freshwater systems

Although no experiments with fresh or pure water were performed in this study, the results can be compared to previous studies. Gysi and Stefansson (2012b) performed two batch experiments at 150 °C, reacting CO_2 charged freshwater with basaltic glass powder of the same origin as in this study (Stapafell, Iceland) at an initial water/rock ratio of 5 for 26 and 123 days, respectively. The DIC concentration of their reactive liquid decreased from ~ 100 to ~55 mM during their 123 day experiment, and to ~70 mM during their 26 day experiment. While this decrease in DIC is of the same magnitude as the CO_2 mineralization rates observed in the present study under comparable conditions (the high-pCO_2 series), the DIC decrease reported by Gysi and Stefansson (2012b) was not exclusively due to carbon mineralization. Gysi and Stefansson (2012b) sampled their batch reactors periodically to monitor the liquid phase composition, thereby increasing the headspace volume. This leads to a degassing of the aqueous solution, lowering its DIC concentration. As a result, the pH of the reactive liquids in the Gysi and Stefansson (2012b) experiments increased to pH 6.4 at the end of their 123 day experiment, while the pH remained close to constant at pH ~5 in our high-pCO_2 experiments. This difference is potentially related to the low Mg concentration of their initial freshwater, such that less clay mineral precipitation occurred. Clay mineral precipitation buffers pH and alkalinity as it liberates protons to the liquid phase (e.g., Voigt et al., 2020). Note, however, that a number of other studies reported substantial clay mineral formation in experiments using freshwater for CO_2 mineralization studies of basalts and anorthite (e.g., Hangx and Spiers, 2009; Munz et al., 2012; Hellevang et al., 2017; Gadikota et al., 2020). A further difference between the seawater and freshwater experiments can be seen in the carbonate mineralogy. While only calcite formation was observed at 150 °C in the freshwater experiments of Gysi and Stefansson (2012b), our study observed calcite formation only in some shorter duration experiments, while the majority of the experiments show mostly aragonite or magnesite formation. This observation is in agreement with field evidence. Carbonate mineral formation during freshwater-basalt-CO_2 interaction during the CarbFix injections (Matter et al., 2016; Snæbjörnsdóttir et al., 2017; Strandmann et al., 2019) is dominated by calcite formation, whereas aragonite formation is predominant in young marine sediments and hydrothermal settings (Coogan and Gillis, 2018). The absence of magnesite in the aforementioned freshwater experiments is most likely due to the lack of Mg in the initial liquid, suggesting that the use of seawater for CO_2 mineralization efforts could be advantageous if the dissolved Mg is consumed by carbonation reactions instead of or along with aluminosilicate formation reactions.

4.5 Implications for mineral carbon storage

The formation of carbonate minerals due to interaction of CO_2-containing seawater with basaltic rocks is a natural process leading to the drawdown and storage of globally significant amounts of CO_2, and thus climate regulation, over geologic timescales (Staudigel et al., 1989; Brady and Gíslason, 1997; Alt and Teagle, 1999; Coogan and Gillis, 2013; Isson et al., 2020). This occurs in low-temperature hydrothermal systems in the basaltic oceanic crust, where carbonate abundances reach up to ~ 4 wt% (e.g., Gillis and Coogan, 2011; Coogan and Gillis, 2013), mostly precipitating during the first 20 million years after crust formation. In this study, we presented experimental evidence that this process can be significantly accelerated by reacting seawater charged with high pCO_2 with basalt at 130 °C, leading to substantial CO_2 mineralization within several months. The effect of different initial conditions, most importantly pCO_2 and seawater composition (standard seawater vs. Mg free seawater), was studied in different sets of experiments. Up to around 20% of the total CO_2 contained in the reactor was mineralized after 5 months both at ~ 2.5 bar and ~ 16 bar initial pCO_2 (26 and 125 mM DIC, respectively). CO_2 mineralization of over 50 % was observed after > 200 days in experiments that started in the presence of ~ 0.1 wt% calcite or run with reduced stirring rates. However, it is unclear how much of this increased mineralization can be attributed to longer run times as opposed to these experimental conditions. Nevertheless, such an effect would be relevant to natural basalt reservoirs containing pre-existing carbonate minerals formed by natural weathering and fluid-rock reactions. In the high-pCO_2 experiments, magnesite was formed as opposed to aragonite at lower initial pCO_2, and significantly less voluminous smectite clay formation was observed. This, in combination with the higher absolute amounts of CO_2 mineralization, makes such conditions particularly attractive for mineral carbon storage applications. Furthermore, a higher initial DIC concentration allows injection of the same quantity of CO_2 with fewer wells due to the reduced amount of liquid injected. This will reduce the significant costs for the drilling of wells.

A temperature of 130 °C was chosen for our experiments to avoid rapid anhydrite formation when seawater is heated to temperatures exceeding 150 °C (Bischoff and Seyfried, 1978). Observations and reaction path modelling suggest only limited anhydrite formation at 130 °C. Therefore, this temperature should be regarded as the upper limit to avoid rapid anhydrite formation that could potentially lead to fluid pathway clogging close to CO_2 injection wells. The Mg-free seawater experiments were designed to see if the formation of voluminous smectite clays could be avoided at low-pCO_2 conditions. This appears to be the case, as zeolites where formed instead of clays, and CO_2 mineralization was higher compared to experiments started with natural seawater (see Figure 8). However, rapid anhydrite precipitation occurs in this case due to the lack of Mg-SO_4 complexation, potentially leading to clogging of fluid pathways close to the injection site.

The magnitude of mineralization observed in the CO_2 charged seawater experiments performed in this study is comparable to that observed in experiments conducted with freshwater (Gysi and Stefánsson, 2012b). This suggests that subsurface carbon storage using seawater, similar to existing injections in freshwater systems (Matter et al., 2016; Clark et al., 2020) is feasible. As opposed to freshwater, injection of CO_2-charged seawater has the advantage of a lower price, much greater availability, and avoidance of potential water use conflicts. Furthermore, vast amounts of CO_2 can be stored in the basaltic oceanic crust; Marieni et al. (2013) estimated that ~ $3x10^5$ Gt CO_2 can be potentially stored in deep-sea basalt at water depths > 5000 m. Finally, offshore storage could reduce public acceptance and political issues associated with onshore CCS projects, as such offshore mineral carbon storage through CO_2-charged seawater injection has the potential to significantly increase the global relevance of such techniques.

The extrapolation of the results of this study to natural and/or engineered subsurface sites is complicated by large uncertainties of reactive surface areas in natural rocks as well as the effect of fluid dynamics on rates. To address such issues, it is common to adjust reaction rates by up to several orders of magnitude when fitting reactive transport models to field results (Aradóttir et al., 2012; Beckingham et al., 2016, 2017). Nevertheless, our experimental results indicate that different initial W/R ratios did not significantly change the amount of CO_2 mineralization (Figure 6, section 4.2). This highlights the importance of secondary mineral precipitation rates as opposed to the reactive surface area of the primary basalt. Therefore, similar timescales of mineralization might be realized on laboratory vs. field scales even if reactive surface areas of the primary rocks are substantially different. Our reaction path models indicate slowing reactions over time during the experiments, which may be due to secondary aluminosilicate precipitation on primary basaltic glass surfaces. Similar processes might occur on field scales. However, it remains to be clarified to what degree secondary mineral precipitation slows mineralization processes over the long term. In the field, the formation of voluminous secondary minerals potentially modifies or clog fluid flow pathways. Evidence from altered oceanic crust, however, suggests that substantial porosity is maintained despite such clogging processes (e.g., Fisher, 1998; Jarrard et al., 2003; Johnson and Pruis, 2003).

5 Conclusions

This study demonstrated the efficiency of carbon mineral formation from CO_2-charged seawater during its interaction with fresh basaltic glass. If a similar efficiency of this reaction can be demonstrated in the field, it may provide a powerful approach for the safe, long-term, and cost-effective storage of CO_2 at many sites around the world. Due to the widespread availability of seawater in the vicinity of basalt and its low cost, such reactions could enable significant upscaling of CCS through mineral carbon storage. CO_2 mineralization of over 30 % was observed in experiments after > 150 days. These rates were potentially further accelerated in the presence of ~ 0.1 wt% calcite seeds. As small quantities of calcite are common in basaltic rocks, such acceleration might be at work in many subsurface systems.

The experimental results also provide insight into the role of non-carbonate secondary minerals in subsurface mineral carbonation efforts. Pore clogging secondary minerals such as smectite can be detrimental to the long-term efforts as they may limit well injectivity over time. Experimental results in this study suggest that the precipitation of such minerals can be delayed or even avoided by controlling the composition of the injected CO_2-charged liquid. Specifically, raising the pCO_2 from ~ 2.5 bar to ~ 16 bar resulted in the formation of magnesite as the exclusive carbonate mineral while smectite formation was largely suppressed. Also, experiments started with synthetic Mg-free seawater resulted in the formation of zeolites instead of clay minerals and higher CO_2 mineralization rates. Further efforts could be made to explore how to best limit the formation of such pore clogging minerals to better exploit subsurface pore space for geologic carbon storage.

Acknowledgements

The authors would like to thank Glúmur Björnsson and Ríkey Kjartansdóttir for help ICP-OES analyses, and Pascale Bénézeth for providing access to the TIC apparatus. We would also like to thank Deirdre Clark and Morgan Jones for providing the ground Stapafell basaltic glass and seawater, respectively. This research has been carried out within the CarbFix2 project that has received funding from the European Union's Horizon 2020 research and innovation program under grant agreement No 764760. The research was also funded by the Loftslagsjóður by the Icelandic government under grant agreement No 200311-5801. Finally, we thank Rachael James for her editorial support as well as Andrew Luhmann and two anonymous reviewers for their insightful reviews.

Bibliography

Alt J. C. and Teagle D. A. H. (1999) The uptake of carbon during alteration of ocean crust. *Geochim. Cosmochim. Acta* **63**, 1527–1535.

Anderson G. M. (1976) Error propagation by the Monte Carlo method in geochemical calculations. *Geochim. Cosmochim. Acta* **40**, 1533–1538.

Aradóttir E. S. P., Sonnenthal E. L., Björnsson G. and Jónsson H. (2012) Multidimensional reactive transport modeling of CO2 mineral sequestration in basalts at the Hellisheidi geothermal field, Iceland. *Int. J. Greenh. Gas Control* **9**, 24–40.

Arnórsson S., Bjarnason J. Ö., Giroud N., Gunnarsson I. and Stefánsson A. (2006) Sampling and analysis of geothermal fluids. *Geofluids* **6**, 203–216.

Baldermann A., Dohrmann R., Kaufhold S., Nickel C., Letofsky-Papst I. and Dietzel M. (2014) The Fe-Mg-saponite solid solution series a hydrothermal synthesis study. *Clay Miner.* **49**, 391–415.

Baldermann A., Mavromatis V., Frick P. M. and Dietzel M. (2018) Effect of aqueous Si/Mg ratio and pH on the nucleation and growth of sepiolite at 25 °C. *Geochim. Cosmochim. Acta* **227**, 211–226.

Baldermann A., Mittermayr F., Bernasconi S. M., Dietzel M., Grengg C., Hippler D., Kluge T., Leis A., Lin K., Wang X., Zünterl A. and Boch R. (2020) Fracture dolomite as an archive of continental palaeo-environmental conditions. *Commun. Earth Environ.* **1**, 1–12.

Beckingham L. E., Mitnick E. H., Steefel C. I., Zhang S., Voltolini M., Swift A. M., Yang L., Cole D. R., Sheets J. M., Ajo-Franklin J. B., DePaolo D. J., Mito S. and Xue Z. (2016) Evaluation of mineral reactive surface area estimates for prediction of reactivity of a multi-mineral sediment. *Geochim. Cosmochim. Acta* **188**, 310–329.

Beckingham L. E., Steefel C. I., Swift A. M., Voltolini M., Yang L., Anovitz L. M., Sheets J. M., Cole D. R., Kneafsey T. J., Mitnick E. H., Zhang S., Landrot G., Ajo-Franklin J. B., DePaolo D. J., Mito S. and Xue Z. (2017) Evaluation of accessible mineral surface areas for improved prediction of mineral reaction rates in porous media. *Geochim. Cosmochim. Acta* **205**, 31–49.

Bénézeth P., Saldi G. D., Dandurand J.-L. and Schott J. (2011) Experimental determination of the solubility product of magnesite at 50 to 200 °C. *Chem. Geol.* **286**, 21–31.

Bischoff J. L. and Seyfried W. E. Jr. (1978) Hydrothermal chemistry of seawater from 25° to 350°C. *Am. J. Sci.* **278**, 838–860.

Brady P. V. and Gíslason S. R. (1997) Seafloor weathering controls on atmospheric CO_2 and global climate. *Geochim. Cosmochim. Acta* **61**, 965–973.

Brunauer S., Emmett P. H. and Teller E. (1938) Adsorption of gases in multimolecular layers. *J. Am. Chem. Soc.* **60**, 309–319.

Clark D. E., Galeczka I. M., Dideriksen K., Voigt M. J., Wolff-Boenisch D. and Gislason S. R. (2019) Experimental observations of CO_2-water-basaltic glass interaction in a large column reactor experiment at 50 °C. *Int. J. Greenh. Gas Control* **89**, 9–19.

Clark D. E., Oelkers E. H., Gunnarsson I., Sigfússon B., Snæbjörnsdóttir S. Ó., Aradóttir E. S. and Gíslason S. R. (2020) CarbFix2: CO_2 and H_2S mineralization during 3.5 years of continuous injection into basaltic rocks at more than 250 °C. *Geochim. Cosmochim. Acta* **279**, 45–66.

Coogan L. A. and Gillis K. M. (2013) Evidence that low-temperature oceanic hydrothermal systems play an important role in the silicate-carbonate weathering cycle and long-term climate regulation. *Geochem. Geophys. Geosystems* **14**, 1771–1786.

Coogan L. A. and Gillis K. M. (2018) Low-Temperature Alteration of the Seafloor: Impacts on Ocean Chemistry. *Annu. Rev. Earth Planet. Sci.* **46**.

Decarreau A., Petit S., Martin F., Farges F., Vieillard P. and Joussein E. (2008) Hydrothermal Synthesis, Between 75 and 150°C, of High-Charge, Ferric Nontronites. *Clays Clay Miner.* **56**, 322–337.

Fisher A. T. (1998) Permeability within basaltic oceanic crust. *Rev. Geophys.* **36**, 143–182.

Friedlingstein P., O'Sullivan M., Jones M. W., Andrew R. M., Hauck J., Olsen A., Peters G. P., Peters W., Pongratz J., Sitch S., Le Quéré C., Canadell J. G., Ciais P., Jackson R. B., Alin S., Aragão L. E. O. C., Arneth A., Arora V., Bates N. R., Becker M., Benoit-Cattin A., Bittig H. C., Bopp L., Bultan S., Chandra N., Chevallier F., Chini L. P., Evans W., Florentie L., Forster P. M., Gasser T., Gehlen M., Gilfillan D., Gkritzalis T., Gregor L., Gruber N., Harris I., Hartung K., Haverd V., Houghton R. A., Ilyina T., Jain A. K., Joetzjer E., Kadono K., Kato E., Kitidis V., Korsbakken J. I., Landschützer P., Lefèvre N., Lenton A., Lienert S., Liu Z., Lombardozzi D., Marland G., Metzl N., Munro D. R., Nabel J. E. M. S., Nakaoka S.-I., Niwa Y., O'Brien K., Ono T., Palmer P. I., Pierrot D., Poulter B., Resplandy L., Robertson E., Rödenbeck C., Schwinger J., Séférian R., Skjelvan I., Smith A. J. P., Sutton A. J., Tanhua T., Tans P. P., Tian H., Tilbrook B., van der Werf G., Vuichard N., Walker A. P., Wanninkhof R., Watson A. J., Willis D., Wiltshire A. J., Yuan W., Yue X. and Zaehle S. (2020) Global Carbon Budget 2020. *Earth Syst. Sci. Data* **12**, 3269–3340.

Gadikota G., Matter J., Kelemen P., Brady P. V. and Park A.-H. A. (2020) Elucidating the differences in the carbon mineralization behaviors of calcium and magnesium bearing alumino-silicates and magnesium silicates for CO_2 storage. *Fuel* **277**, 117900.

Galeczka I., Wolff-Boenisch D., Jonsson T., Sigfusson B., Stefansson A. and Gislason S. R. (2013) A novel high pressure column flow reactor for experimental studies of CO_2 mineral storage. *Appl. Geochem.* **30**, 91–104.

Galeczka I., Wolff-Boenisch D., Oelkers E. H. and Gislason S. R. (2014) An experimental study of basaltic glass–H_2O–CO_2 interaction at 22 and 50°C: Implications for subsurface storage of CO_2. *Geochim. Cosmochim. Acta* **126**, 123–145.

Gillis K. M. and Coogan L. A. (2011) Secular variation in carbon uptake into the ocean crust. *Earth Planet. Sci. Lett.* **302**, 385–392.

Gillis K. M., Muehlenbachs K., Stewart M., Gleeson T. and Karson J. (2001) Fluid flow patterns in fast spreading East Pacific Rise crust exposed at Hess Deep. *J. Geophys. Res. Solid Earth* **106**, 26311–26329.

Gíslason S. R., Heaney P. J., Oelkers E. H. and Schott J. (1997) Kinetic and thermodynamic properties of moganite, a novel silica polymorph. *Geochim. Cosmochim. Acta* **61**, 1193–1204.

Gíslason S. R. and Oelkers E. H. (2003) Mechanism, rates, and consequences of basaltic glass dissolution: II. An experimental study of the dissolution rates of basaltic glass as a function of pH and temperature. *Geochim. Cosmochim. Acta* **67**, 3817–3832.

Global CCS Institute (2020) *Global Status of CCS 2020*.,

Gran G. (1952) Determination of the equivalence point in potentiometric titrations. Part II. *Analyst* **77**, 661–671.

Gunnarsson I., Aradóttir E. S., Oelkers E. H., Clark D. E., Arnarson M. Þ., Sigfússon B., Snæbjörnsdóttir S. Ó., Matter J. M., Stute M., Júlíusson B. M. and Gíslason S. R. (2018) The rapid and cost-effective capture and subsurface mineral storage of carbon and sulfur at the CarbFix2 site. *Int. J. Greenh. Gas Control* **79**, 117–126.

Gysi A. P. and Stefánsson A. (2012a) CO_2-water–basalt interaction. Low temperature experiments and implications for CO_2 sequestration into basalts. *Geochim. Cosmochim. Acta* **81**, 129–152.

Gysi A. P. and Stefánsson A. (2012b) Experiments and geochemical modeling of CO_2 sequestration during hydrothermal basalt alteration. *Chem. Geol.* **306–307**, 10–28.

Gysi A. P. and Stefánsson A. (2012c) Mineralogical aspects of CO_2 sequestration during hydrothermal basalt alteration — An experimental study at 75 to 250 °C and elevated pCO_2. *Chem. Geol.* **306–307**, 146–159.

Hangx S. J. T. and Spiers C. J. (2009) Reaction of plagioclase feldspars with CO_2 under hydrothermal conditions. *Chem. Geol.* **265**, 88–98.

Heft K. L., Gillis K. M., Pollock M. A., Karson J. A. and Klein E. M. (2008) Role of upwelling hydrothermal fluids in the development of alteration patterns at fast spreading ridges: Evidence from the sheeted dike complex at Pito Deep. *Geochem. Geophys. Geosystems* **9**.

Hellevang H., Haile B. G. and Tetteh A. (2017) Experimental study to better understand factors affecting the CO_2 mineral trapping potential of basalt. *Greenh. Gases Sci. Technol.* **7**, 143–157.

Isson T. T., Planavsky N. J., Coogan L. A., Stewart E. M., Ague J. J., Bolton E. W., Zhang S., McKenzie N. R. and Kump L. R. (2020) Evolution of the Global Carbon Cycle and Climate Regulation on Earth. *Glob. Biogeochem. Cycles* **34**, e2018GB006061.

Jarrard R. D., Abrams L. J., Pockalny R., Larson R. L. and Hirono T. (2003) Physical properties of upper oceanic crust: Ocean Drilling Program Hole 801C and the waning of hydrothermal circulation. *J. Geophys. Res. Solid Earth* **108**.

Johnson H. P. and Pruis M. J. (2003) Fluxes of fluid and heat from the oceanic crustal reservoir. *Earth Planet. Sci. Lett.* **216**, 565–574.

Jones M. T., Pearce C. R., Jeandel C., Gíslason S. R., Eiriksdottir E. S., Mavromatis V. and Oelkers E. H. (2012) Riverine particulate material dissolution as a significant flux of strontium to the oceans. *Earth Planet. Sci. Lett.* **355–356**, 51–59.

Kaasalainen H. and Stefánsson A. (2011) Sulfur speciation in natural hydrothermal waters, Iceland. *Geochim. Cosmochim. Acta* **75**, 2777–2791.

Kleine B. I., Stefánsson A., Kjartansdóttir R., Prause S., Weisenberger T. B., Reynolds H. I., Sveinbjörnsdóttir Á. E., Jackson M. D. and Gudmundsson M. T. (2020) The Surtsey volcano geothermal system: An analogue for seawater-oceanic crust interaction with implications for the elemental budget of the oceanic crust. *Chem. Geol.* **550**, 119702.

Kumar A., Shrivastava J. P. and Pathak V. (2017) Mineral carbonation reactions under water-saturated, hydrothermal-like conditions and numerical simulations of CO_2 sequestration in tholeiitic basalt of the Eastern Deccan Volcanic Province, India. *Appl. Geochem.* **84**, 87–104.

Luhmann A. J., Tutolo B. M., Tan C., Moskowitz B. M., Saar M. O. and Seyfried W. E. (2017) Whole rock basalt alteration from CO_2-rich brine during flow-through experiments at 150 °C and 150 bar. *Chem. Geol.* **453**, 92–110.

Marieni C., Henstock T. J. and Teagle D. A. H. (2013) Geological storage of CO_2 within the oceanic crust by gravitational trapping. *Geophys. Res. Lett.* **40**, 2013GL058220.

Marieni C., Matter J. M. and Teagle D. A. H. (2020) Experimental study on mafic rock dissolution rates within CO_2-seawater-rock systems. *Geochim. Cosmochim. Acta* **272**, 259–275.

Marks N., Schiffman P., Zierenberg R. A., Franzson H. and Fridleifsson G. Ó. (2010) Hydrothermal alteration in the Reykjanes geothermal system: Insights from Iceland deep drilling program well RN-17. *J. Volcanol. Geotherm. Res.* **189**, 172–190.

Matter J. M., Stute M., Snæbjörnsdottir S. Ó., Oelkers E. H., Gislason S. R., Aradottir E. S., Sigfusson B., Gunnarsson I., Sigurdardottir H., Gunnlaugsson E., Axelsson G., Alfredsson H. A., Wolff-Boenisch D., Mesfin K., Taya D. F. de la R., Hall J., Dideriksen K. and Broecker W. S. (2016) Rapid carbon mineralization for permanent disposal of anthropogenic carbon dioxide emissions. *Science* **352**, 1312–1314.

McGrail B. P., Schaef H. T., Spane F. A., Cliff J. B., Qafoku O., Horner J. A., Thompson C. J., Owen A. T. and Sullivan C. E. (2017) Field Validation of Supercritical CO_2 Reactivity with Basalts. *Environ. Sci. Technol. Lett.* **4**, 6–10.

Menefee A. H., Giammar D. E. and Ellis B. R. (2018) Permanent CO_2 Trapping through Localized and Chemical Gradient-Driven Basalt Carbonation. *Environ. Sci. Technol.* **52**, 8954–8964.

Menefee A. H., Li P., Giammar D. E. and Ellis B. R. (2017) Roles of Transport Limitations and Mineral Heterogeneity in Carbonation of Fractured Basalts. *Environ. Sci. Technol.* **51**, 9352–9362.

Millero F. J., Feistel R., Wright D. G. and McDougall T. J. (2008) The composition of standard seawater and the definition of the reference-composition salinity scale. *Deep Sea Res. Part Oceanogr. Res. Pap.* **55**, 50–72.

Morse J. W., Wang Q. and Tsio M. Y. (1997) Influences of temperature and Mg:Ca ratio on $CaCO_3$ precipitates from seawater. *Geology* **25**, 85–87.

Mottl M. J. and Holland H. D. (1978) Chemical exchange during hydrothermal alteration of basalt by seawater—I. Experimental results for major and minor components of seawater. *Geochim. Cosmochim. Acta* **42**, 1103–1115.

Mottl M. J., Holland H. D. and Corr R. F. (1979) Chemical exchange during hydrothermal alteration of basalt by seawater—II. Experimental results for Fe, Mn, and sulfur species. *Geochim. Cosmochim. Acta* **43**, 869–884.

Munz I. A., Brandvoll Ø., Haug T. A., Iden K., Smeets R., Kihle J. and Johansen H. (2012) Mechanisms and rates of plagioclase carbonation reactions. *Geochim. Cosmochim. Acta* **77**, 27–51.

Oelkers E. H. and Gíslason S. R. (2001) The mechanism, rates and consequences of basaltic glass dissolution: I. An experimental study of the dissolution rates of basaltic glass as a function of aqueous Al, Si and oxalic acid concentration at 25 °C and pH= 3 and 11. *Geochim. Cosmochim. Acta* **65**, 3671–3681.

Parkhurst D. L. and Appelo C. A. J. (2013) Description of input and examples for PHREEQC version 3 - A computer program for speciation, batch-reaction, one-dimensional transport, and inverse geochemical calculations. In *U.S. Geological Survey techniques* *and methods, modeling techniques, groundwater* U.S. Geological Survey, Denver, Colorado.

Přikryl J., Marieni C., Gudbrandsson S., Aradóttir E. S., Gunnarsson I. and Stefánsson A. (2018) H_2S sequestration process and sustainability in geothermal systems. *Geothermics* **71**, 156–166.

Rigopoulos I., Harrison A. L., Delimitis A., Ioannou I., Efstathiou A. M., Kyratsi T. and Oelkers E. H. (2017) Carbon sequestration via enhanced weathering of peridotites and basalts in seawater. *Appl. Geochem.*

Rogelj J., Shindell D., Jiang K., Fifita S., Forster P., Ginzburg V., Handa C., Kheshgi H., Kobayashi S., Kriegler E., Mundaca L., Seferian R., Vilarino M. V., Calvin K., Edelenbosch O., Emmerling J., Fuss S., Gasser T., Gillet N., He C., Hertwich E., Höglund Isaksson L., Huppmann D., Luderer G., Markandya A., McCollum D., Millar R., Meinshausen M., Popp A., Pereira J., Purohit P., Riahi K., Ribes A., Saunders H., Schadel C., Smith C., Smith P., Trutnevyte E., Xiu Y., Zickfeld K. and Zhou W. (2018) Chapter 2: Mitigation pathways compatible with 1.5°C in the context of sustainable development. In *Global Warming of 1.5 °C - an IPCC special report on the impacts of global warming of 1.5 °C above pre-industrial levels and related global greenhouse gas emission pathways, in the context of strengthening the global response to the threat of climate change* Intergovernmental Panel on Climate Change.

Rosenbauer R. J., Thomas B., Bischoff J. L. and Palandri J. (2012) Carbon sequestration via reaction with basaltic rocks: Geochemical modeling and experimental results. *Geochim. Cosmochim. Acta* **89**, 116–133.

Sand K. K., Rodriguez-Blanco J. D., Makovicky E., Benning L. G. and Stipp S. L. S. (2012) Aragonite growth in water-alcohol mixtures: Classical or nonclassical crystallization? *MRS Online Proc. Libr. Arch.* **1419**.

Seyfried W. E. Jr. (1977) Seawater-basalt interaction from 25°-300°C and 1-500 bars: Implications for the origin of submarine metal-bearing hydrothermal solutions and regulation of ocean chemistry. PhD Thesis, University of Southern California.

Seyfried W. E. Jr. and Bischoff J. L. (1981) Experimental seawater-basalt interaction at 300°C, 500 bars, chemical exchange, secondary mineral formation and implications for the transport of heavy metals. *Geochim. Cosmochim. Acta* **45**, 135–147.

Seyfried W. E. Jr. and Bischoff J. L. (1979) Low temperature basalt alteration by sea water: an experimental study at 70 °C and 150 °C. *Geochim. Cosmochim. Acta* **43**, 1937–1947.

Seyfried W. E. Jr. and Mottl M. J. (1982) Hydrothermal alteration of basalt by seawater under seawater-dominated conditions. *Geochim. Cosmochim. Acta* **46**, 985–1002.

Shibuya T., Yoshizaki M., Masaki Y., Suzuki K., Takai K. and Russell M. J. (2013) Reactions between basalt and CO_2-rich seawater at 250 and 350°C, 500bars: Implications for the CO_2 sequestration into the modern oceanic crust and the composition of hydrothermal vent fluid in the CO_2-rich early ocean. *Chem. Geol.* **359**, 1–9.

Snæbjörnsdóttir S. Ó., Oelkers E. H., Mesfin K., Aradóttir E. S., Dideriksen K., Gunnarsson I., Gunnlaugsson E., Matter J. M., Stute M. and Gislason S. R. (2017) The chemistry and saturation states of subsurface fluids during the in situ mineralisation of CO_2 and H_2S at the CarbFix site in SW-Iceland. *Int. J. Greenh. Gas Control* **58**, 87–102.

Snæbjörnsdóttir S. Ó., Sigfússon B., Marieni C., Goldberg D., Gislason S. R. and Oelkers E. H. (2020) Carbon dioxide storage through mineral carbonation. *Nat. Rev. Earth Environ.* **1**, 90–102.

Stanley S. M. and Hardie L. A. (1999) Hypercalcification: paleontology links plate tectonics and geochemistry to sedimentology. *GSA Today* **9**, 1–7.

Stanley S. M. and Hardie L. A. (1998) Secular oscillations in the carbonate mineralogy of reef-building and sediment-producing organisms driven by tectonically forced shifts in seawater chemistry. *Palaeogeogr. Palaeoclimatol. Palaeoecol.* **144**, 3–19.

Staudigel H., Hart S. R., Schmincke H.-U. and Smith B. M. (1989) Cretaceous ocean crust at DSDP Sites 417 and 418: Carbon uptake from weathering versus loss by magmatic outgassing. *Geochim. Cosmochim. Acta* **53**, 3091–3094.

Stockmann G. J., Wolff-Boenisch D., Bovet N., Gislason S. R. and Oelkers E. H. (2014) The role of silicate surfaces on calcite precipitation kinetics. *Geochim. Cosmochim. Acta* **135**, 231–250.

Stockmann G. J., Wolff-Boenisch D., Gíslason S. R. and Oelkers E. H. (2013) Do carbonate precipitates affect dissolution kinetics? 2: Diopside. *Chem. Geol.* **337–338**, 56–66.

Strandmann P. A. E. P. von, Burton K. W., Snæbjörnsdóttir S. O., Sigfússon B., Aradóttir E. S., Gunnarsson I., Alfredsson H. A., Mesfin K. G., Oelkers E. H. and Gislason S. R. (2019) Rapid CO_2 mineralisation into calcite at the CarbFix storage site quantified using calcium isotopes. *Nat. Commun.* **10**, 1–7.

Stumm W. and Morgan J. J. (1996) *Aquatic Chemistry: Chemical Equilibria and Rates in Natural Waters*. 3rd Edition., Wiley-Interscience, New York.

Tagirov B. and Schott J. (2001) Aluminum speciation in crustal fluids revisited. *Geochim. Cosmochim. Acta* **65**, 3965–3992.

Voigt M., Marieni C., Clark D. E., Gíslason S. R. and Oelkers E. H. (2018a) Evaluation and refinement of thermodynamic databases for mineral carbonation. *Energy Procedia* **146**, 81–91.

Voigt M., Pearce C. R., Baldermann A. and Oelkers E. H. (2018b) Stable and radiogenic strontium isotope fractionation during hydrothermal seawater-basalt interaction. *Geochim. Cosmochim. Acta* **240**, 131–151.

Voigt M., Pearce C. R., Fries D. M., Baldermann A. and Oelkers E. H. (2020) Magnesium isotope fractionation during hydrothermal seawater-basalt interaction. *Geochim. Cosmochim. Acta* **272**, 21–35.

Wallmann K., Aloisi G., Haeckel M., Tishchenko P., Pavlova G., Greinert J., Kutterolf S. and Eisenhauer A. (2008) Silicate weathering in anoxic marine sediments. *Geochim. Cosmochim. Acta* **72**, 2895–2918.

White S. K., Spane F. A., Schaef H. T., Miller Q. R. S., White M. D., Horner J. A. and McGrail B. P. (2020) Quantification of CO_2 Mineralization at the Wallula Basalt Pilot Project. *Environ. Sci. Technol.* **54**, 14609–14616.

Wiese F., Fridriksson T. and Ármansson H. (2008) *CO_2 fixation by calcite in high-temperature geothermal systems in Iceland*., Íslenskar orkurannsóknir.

Wolff-Boenisch D. and Galeczka I. M. (2018) Flow-through reactor experiments on basalt-(sea)water-CO_2 reactions at 90 °C and neutral pH. What happens to the basalt pore space under post-injection conditions? *Int. J. Greenh. Gas Control* **68**, 176–190.

Wolff-Boenisch D., Galeczka I. M., Mesfin K. G. and Gislason S. R. (2016) A foray into false positive results in mineral dissolution and precipitation studies. *Appl. Geochem.* **71**, 9–19.

Wolff-Boenisch D., Wenau S., Gíslason S. R. and Oelkers E. H. (2011) Dissolution of basalts and peridotite in seawater, in the presence of ligands, and CO_2: Implications for mineral sequestration of carbon dioxide. *Geochim. Cosmochim. Acta* **75**, 5510–5525.

Wolkersdorfer C. (2008) *Water management at abandoned flooded underground mines: fundamentals, tracer tests, modelling, water treatment*., Springer Science & Business Media.

Tables

Table 1: Summary of previous experimental studies on basalt-CO_2-seawater or NaCl-brine interaction.

Study	Reactor type	Aqueous matrix	T / °C	DIC / mM	pH	Carbonate precipitation
Brady and Gíslason (1997)	Flow-through	Seawater	25-50	~ 0.01 – 0.1		No
Wolff-Boenisch et al. (2011)	Mixed flow	Seawater	25	~ 100	3.6	No
Rosenbauer et al. (2012)	Reaction cell	NaCl brine	50 – 200	1000		Magnesite
Shibuya et al. (2013)	Reaction cell	NaCl brine	250, 350	400	7.6, 8.7	Calcite
Luhmann et al. (2017)	Flow-through	NaCl brine	150	650	3.3	Siderite indicated by modelling
Rigopoulos et al. (2017)	Batch reactor	Seawater	~ 25	< 1	8.6	Aragonite
Wolff-Boenisch and Galeczka (2018)	Mixed flow	Seawater	90	40 – 400	7 – 7.7	Calcite, magnesite, Ca/Mg-carbonates
Marieni et al. (2020)	Batch reactor	Seawater	40	~ 30	~ 4.7	No

Table 2: Initial conditions of all experiments with their durations. W/R = water/rock ratio.

Exp.	Duration / days	T / °C	P_{Start} / bar	$p\mathrm{CO}_{2,\mathrm{Start}}$ / bar	pH[a]	SW / g	Basalt / g	W/R	Alk. / meq/kg
Low-0.1[b]	0.08	130	4.81	2.54	5.10	216	86.0	2.5	2.24
Low-5	5	130	4.89	2.63	5.09	230	46.1	5.0	2.24
Low-19	19	130	4.65	2.38	5.13	461	92.0	5.0	2.24
Low-44	44	130	4.59	2.32	5.18	461	92.1	5.0	2.46
Low-57	57	130	4.70	2.43	5.12	461	92.0	5.0	2.25
Low-102	102	130	4.71	2.44	5.13	214	86.0	2.5	2.29
Low-148	148	130	4.78	2.51	5.12	230	46.0	5.0	2.29
Low-150	150	130	5.02	2.75	5.07	216	86.0	2.5	2.25
High-56	56	130	18.22	15.81	4.35	216	86.0	2.5	2.25
High-140	140	130	18.11	15.69	4.35	216	86.1	2.5	2.22
MgFree-60[e]	60	130	4.77	2.49	5.21	461	92.0	5.0	2.25
MgFree-150[e]	150	130	4.73	2.46	5.21	216	86.4	2.5	2.25
Low-66-146	66,146	130	4.48	2.22	5.17	462	92.0	5.0	2.29
Low-$p\mathrm{CO}_2$-Slow[d]	204	130	4.64	2.38	5.12	217	86.0	2.5	2.16
Low-$p\mathrm{CO}_2$-Calcite[c]	228	130	4.94	2.67	5.09	215	86.0	2.5	2.29

[a] Calculated for experimental conditions from P_{Start}, alkalinity, liquid composition, and thermodynamic relationships. [b] Experiment stopped after ~ 2 h to estimate amount of basalt dissolution during CO_2 addition, before reactors were completely sealed [c] 102 mg calcite seed crystals (Riedel-de Haën puriss. p.a.) were added to the reactor. [d] Stirring rate was decreased to 20 rpm after 69 days. [e] synthetic Mg-free seawater was used as the initial reactive liquid

Table 3: Compositions of initial liquids used as reactant and aqueous solutions in mM sampled at the end of each batch experiment. pH and pE are given for *in situ* conditions. Uncertainties of values are approximately ± 3% (95% confidence interval) of their values except for alkalinity (± 0.5%), pH (± 0.06), DIC (± 3 mM), pE (± 0.2), and explicitly stated uncertainties for Fe and Al. Quantification limits were ~ 4 μM for Al, ~ 1 μM for Fe, ~ 0.02 mM for Si, and ~ 1 μM for S^{II-}, below which values are shown as 'BQL'. NA = not analyzed.

Sample	Na	Mg	S^{VI}	Ca	K	Si	Fe	±	Al	±	S^{II-}	Cl	F	Alk. / meq/kg	DIC	pH	pE
Initial Seawater	513	54	28.9	10.3	10.6	BQL	BQL	BQL	BQL	BQL	NA	584	0.040				
Synthetic Mg-free SW	452	0.0114	26.7	9.4	10.5	BQL	BQL	BQL	BQL	BQL	NA	429	0.051				
Low-0.1	524	54	29.6	12.8	10.5	2.82	0.082	0.002	BQL	BQL	NA	598	0.045	7.33	27	5.61	NA
Low-5	548	54	29.2	14.5	11.1	3.11	0.0174	0.0006	0.0078	0.0004	NA	614	0.227	7.27	28	5.58	4.22
Low-19	540	44	20.7	16.0	11.0	3.17	0.0321	0.001	BQL	BQL	NA	606	0.017	8.55	26	5.72	4.87
Low-44	541	32.0	16.1	23.4	10.9	3.4	0.037	0.001	BQL	BQL	NA	604	0.009	7.37	25	5.66	NA
Low-57	520	29.3	13.7	22.4	10.7	3.4	0.0317	0.0010	BQL	BQL	BQL	591	0.010	7.12	24	5.66	5.23
Low-102	574	24.3	9.8	26.4	11.8	3.5	0.0339	0.001	0.00099	0.0002	NA	662	0.016	4.86	21	5.50	3.28
Low-148	568	24.0	10.0	25.1	11.7	3.7	0.0304	0.0010	BQL	BQL	NA	650	0.016	4.37	21	5.45	NA
Low-150	556	27.7	19.3	30.9	11.2	3.8	0.056	0.002	BQL	BQL	NA	626	0.014	5.72	21	5.60	4.65
High-56	528	50	26.1	10.9	10.5	5.4	0.170	0.005	BQL	BQL	BQL	614	0.082	10.90	121	5.04	5.03
High-140	524	46	16.1	12.3	10.3	6.6	0.189	0.006	BQL	BQL	BQL	618	0.101	9.38	105	5.03	1.73
MgFree-60	490	4.2	23.3	3.5	10.6	3.15	0.00278	0.0001	BQL	BQL	BQL	461	0.113	8.35	24	5.87	4.65
MgFree-150	543	5.4	25.9	8.3	11.7	3.9	0.036	0.001	0.0112	0.0005	BQL	502	0.897	9.24	27	5.83	-0.16
Low-66	536	30.1	16.4	26.5	10.6	3.9	0.036	0.001	0.00171	0.0002	NA	627	0.010	6.60	22	5.67	NA
Low-146	570	19.4	13.2	31.4	11.2	3.7	0.0265	0.0008	BQL	BQL	NA	644	0.008	4.14	14	5.66	1.73
Low-pCO_2-Slow	506	16.2	6.9	25.8	11.4	3.5	0.0314	0.0010	BQL	BQL	0.0095	591	0.011	3.51	12	5.66	0.19
Low-pCO_2-Calcite	583	17.3	17.0	41	11.7	4.3	0.040	0.001	BQL	BQL	NA	698	0.041	5.15	17	5.66	NA

Table 4: Total inorganic carbon (TIC) contained in the solids retrieved at the end of each batch experiment, expressed as wt% of the solid and as the percentage of the original total CO_2 in the reactor contained in the solids at the end of the experiment. Values were measured by acidification and NDIR, heating in a furnace and solid state IR, and estimated by mass balance calculations (see text). Relative uncertainties for the acidification method are ~ 6%. BDL = Below detection limit; NA = not analyzed; Acidif. = Acidification.

Exp.	CO_2 / wt% of solids					CO_2 mineralization / %				
	Acidif.	Furnace	±	Mass balance	±	Acidif.	Furnace	±	Mass balance	±
Initial	0.00133	BDL	BDL							
Low-0.1	0.00026	BDL	BDL	0.00	0.03	0.053	BDL	2	0	6
Low-5	0.00020	BDL	BDL	0.00	0.06	0.021	BDL	BDL	0	5
Low-19	0.00049	BDL	BDL	0.01	0.05	0.057	BDL	BDL	1	6
Low-44	0.056	0.08	0.02	0.02	0.05	6.6	9	3	2	7
Low-57	0.044	0.08	0.02	0.06	0.06	5.0	9	3	7	6
Low-102	0.073	0.12	0.03	0.08	0.03	15.4	25	6	17	5
Low-148	0.084	BDL	BDL	0.18	0.06	9.0	BDL	BDL	19	5
Low-150	0.099	0.23	0.04	0.14	0.04	19	44	8	28	5
High-56	NA	0.09	0.03	0.14	0.05	NA	3.5	1.0	5	1
High-140	NA	0.37	0.05	0.44	0.10	NA	14	2	17	1
MgFree-60	0.0166	0.12	0.03	0.14	0.06	1.8	13	3	16	6
MgFree-150	0.155	0.15	0.03	0.02	0.03	33	32	7	3	6
Low-66-146	0.147	0.03	0.01	0.14	0.06	18	4	2	17	6
Low-pCO$_2$-Slow	0.100	0.16	0.03	0.24	0.05	22	35	8	53	4
Low-pCO$_2$-Calcite	0.27	0.31	0.05	0.26	0.05	48	55	9	47	3

Figures

Figure 1: Schematic illustration of the reactor assemblage used for experiments in this study.

Figure 2: Composition of reacted seawater after its interaction with basalt powder and CO_2 at 130 °C in batch experiment of various durations. pH and DIC were calculated from measured alkalinity and pressure for *in situ* temperature conditions. The arrows show major trends observed in the compositions. Note that individual experiments were run at distinct conditions varying initial pCO$_2$, seawater composition, and stirring rate accounting for some of the scatter among these trends. Analytical uncertainties (95% confidence level) are smaller than the symbol size in all cases.

Figure 3: Redox potential, reported as pE, of the sampled reactive liquids, re-calculated for *in situ* temperature conditions, and fraction of Fe^{2+} in total Fe in these reactive liquids calculated based on this redox potential assuming thermodynamic equilibrium. The dashed line shows the Fe^{2+} fraction of the dissolving basaltic glass. Analytical uncertainties (95% confidence interval) are similar to the symbol size.

Figure 4: Secondary electron microscopy (SEM) microphotographs of (A) the initial basaltic glass powder used as reactant, and the solid reaction products collected after experiments (B,C) Low-148, (D) High-140, (E) Low-148, and (F) Low-66-146. The last image also shows an overlay of the morphology of pseudohexagonal aragonite twins, modified after Sand et al. (2012).

Figure 5: Diagram showing the development of alteration and pristine minerals identified in the basalt powder after each experiment by XRD and SEM. In all samples, the majority of the solids was amorphous material (basaltic glass, not shown), while the phases shown in the diagram were present in minor to moderate amounts.

Figure 6: Comparison of total inorganic carbon (TIC) content in the solids determined after each batch experiment, expressed as percentage of total initial carbon present in reactor (a) as measured by NDIR after acidification, (b) as measured by solid state IR after heating in a furnace, and (c) as estimated by fluid mass balance calculations (see text for details). Shown confidence intervals (95%) of mass balance calculations are those propagated from measured values (mainly pressure, alkalinity) using Monte Carlo methods.

Figure 7: Calculated saturation indices (SI) of the reacted liquids collected at the end of each batch experiment with respect to selected alteration minerals. For ankerite and siderite, it was assumed that all aqueous Fe was present as Fe^{II} (see Figure 3 and text). Uncertainties (95% confidence level) propagated from analytical uncertainties are smaller than the symbol size in all cases. Maximum SI of minerals containing Al are presented in Figure S-4 in the Supplementary Material.

Figure 8: Results of reaction path calculations of basalt-seawater-CO_2 interaction at the experimental conditions of this study (initial water/rock ratio of 5 at 130 °C). Reaction progress is shown as function of basalt dissolution in units of g of basaltic glass dissolved per kg seawater (kgw). The length of the horizontal axis corresponds to the mass of basaltic glass dissolved during the ~ 5-month duration of the longest experiments. Note the difference scale of the horizontal axis in the three experimental series. The top plots show the predicted change in solid volume in cm^3 per kgw; the middle plots show the calculated percentage of initial total CO_2 mineralized and the bottom plots show the total g of CO_2 mineralized per kgw. The symbols show the observed percentage of CO_2 mineralized as determined from the CO_2 content of the solids collected at the end of the batch experiments reported in this study by acidification (low pCO_2 and Mg free experiments) and heating methods (high pCO_2 experiments).

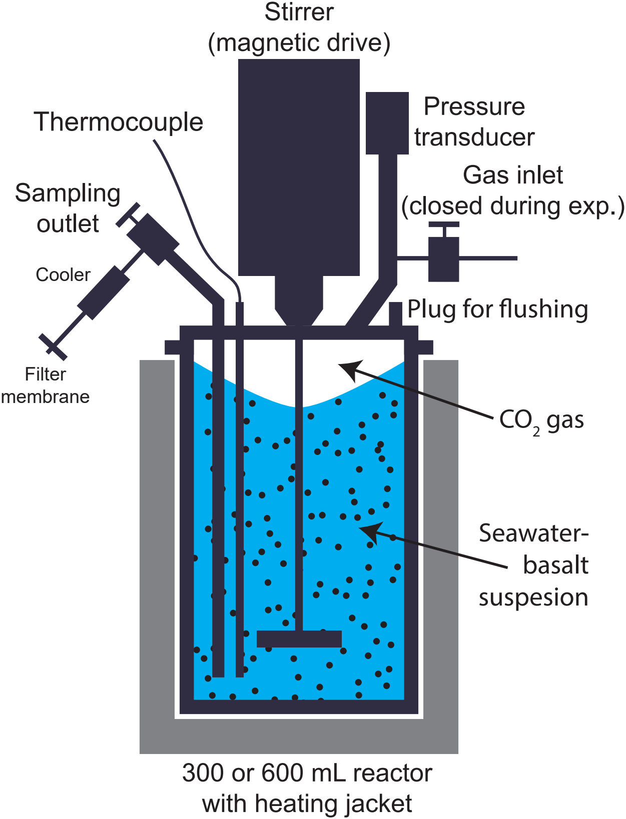
Stirrer
(magnetic drive)
Thermocouple
Pressure transducer
Gas inlet (closed during exp.)
Sampling outlet
Cooler
Plug for flushing
Filter membrane
CO_2 gas
Seawater-basalt suspesion
300 or 600 mL reactor with heating jacket

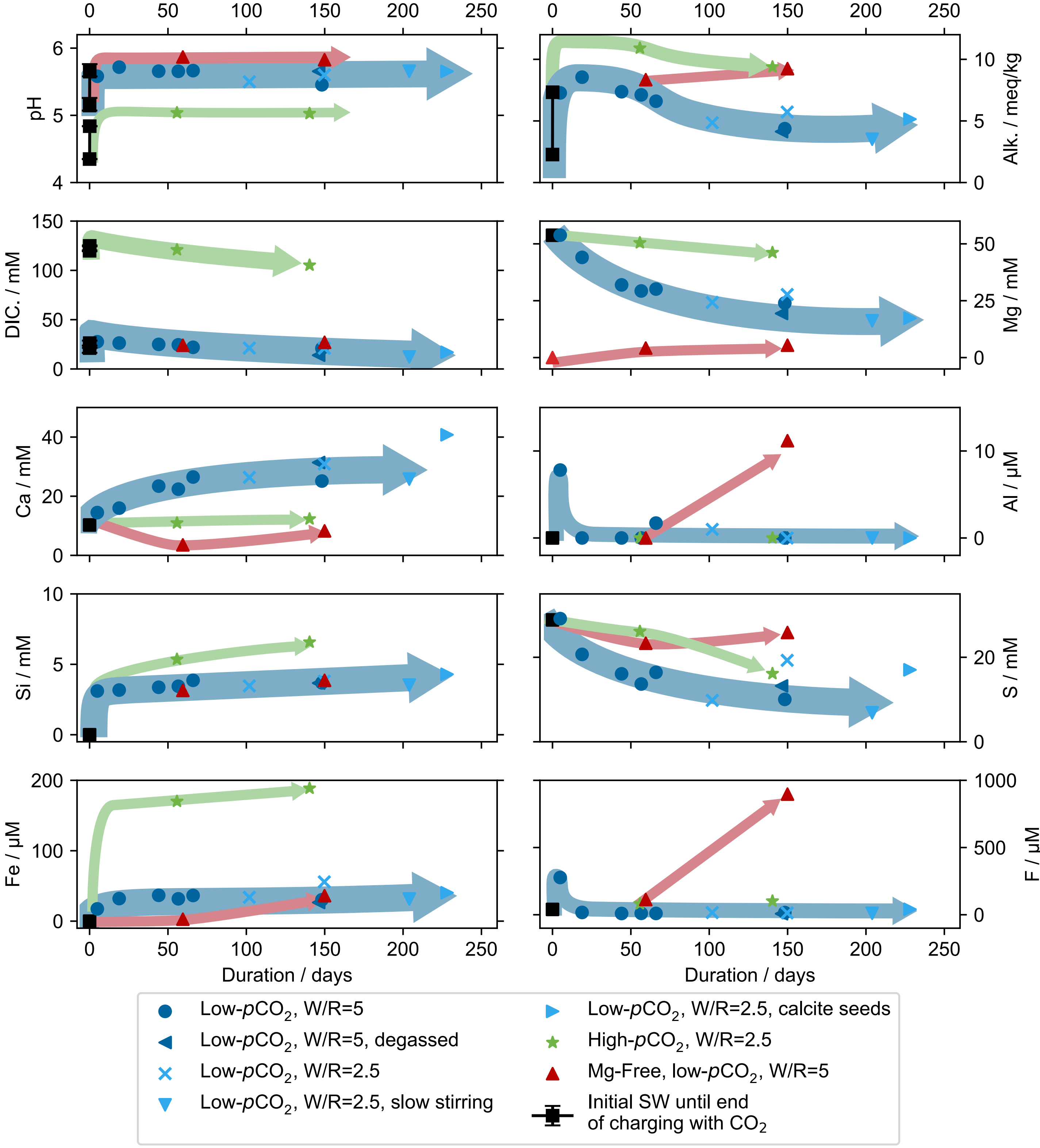
0
50
100
150
200
250
pH
6
5
4
Alk. / meq/kg
10
5
0
DIC. / mM
150
100
50
0
Mg / mM
50
25
0
Ca / mM
40
20
0
Al / µM
10
0
Si / mM
10
5
0
S / mM
20
0
Fe / µM
200
100
0
F / µM
1000
500
0
Duration / days
Duration / days
Low-$p\mathrm{CO_2}$, W/R=5
Low-$p\mathrm{CO_2}$, W/R=5, degassed
Low-$p\mathrm{CO_2}$, W/R=2.5
Low-$p\mathrm{CO_2}$, W/R=2.5, slow stirring
Low-$p\mathrm{CO_2}$, W/R=2.5, calcite seeds
High-$p\mathrm{CO_2}$, W/R=2.5
Mg-Free, low-$p\mathrm{CO_2}$, W/R=5
Initial SW until end of charging with $\mathrm{CO_2}$

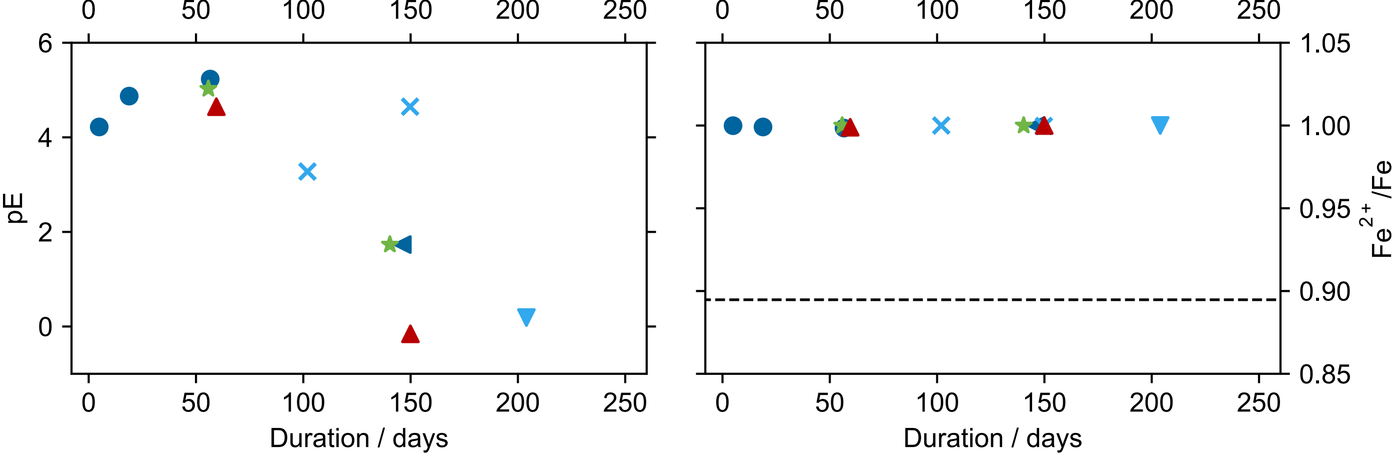
0
50
100
150
200
250
6
4
2
0
pE
Duration / days
1.05
1.00
0.95
0.90
0.85
Fe^{2+}/Fe

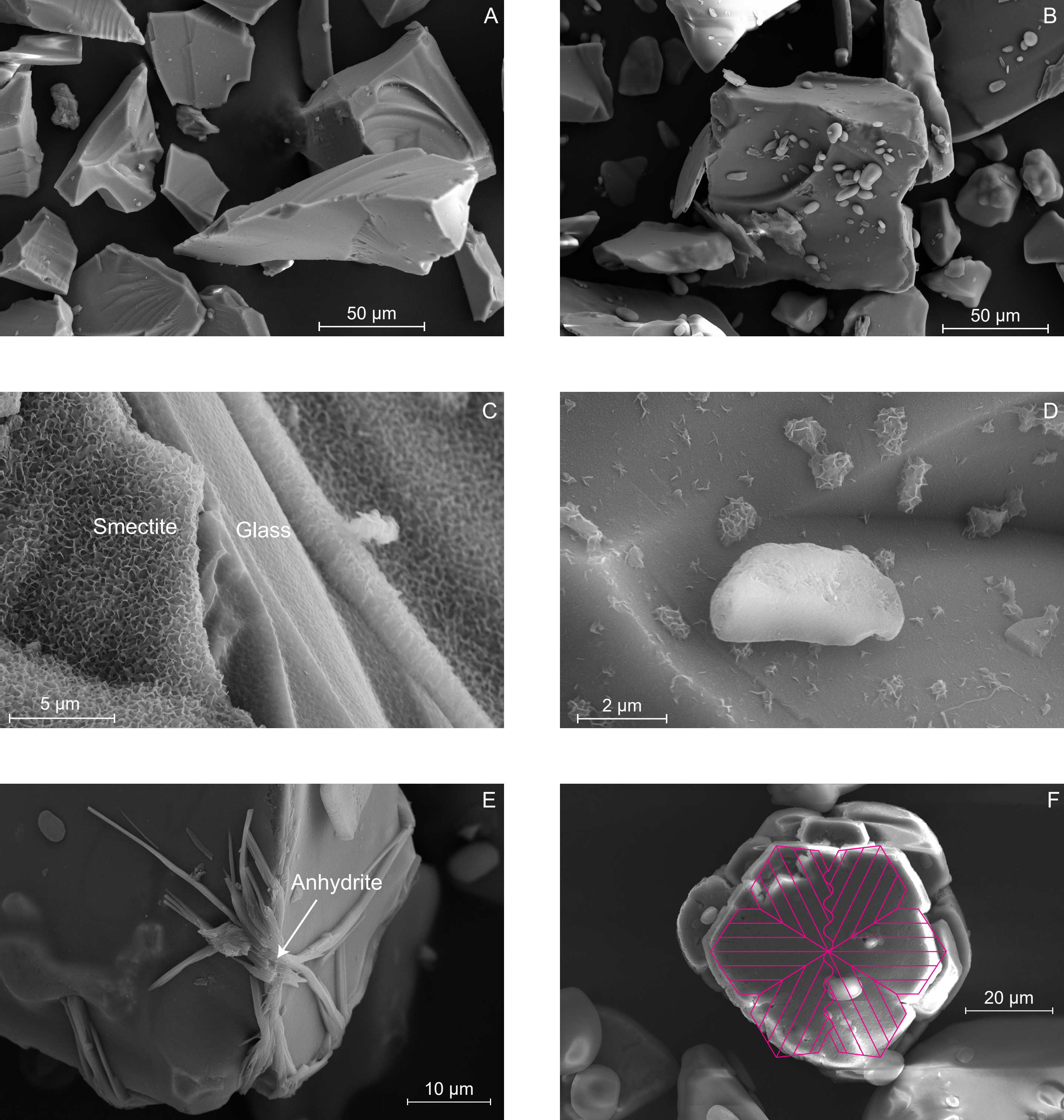
A
50 µm
B
50 µm
C
Smectite
Glass
5 µm
D
2 µm
E
Anhydrite
10 µm
F
20 µm

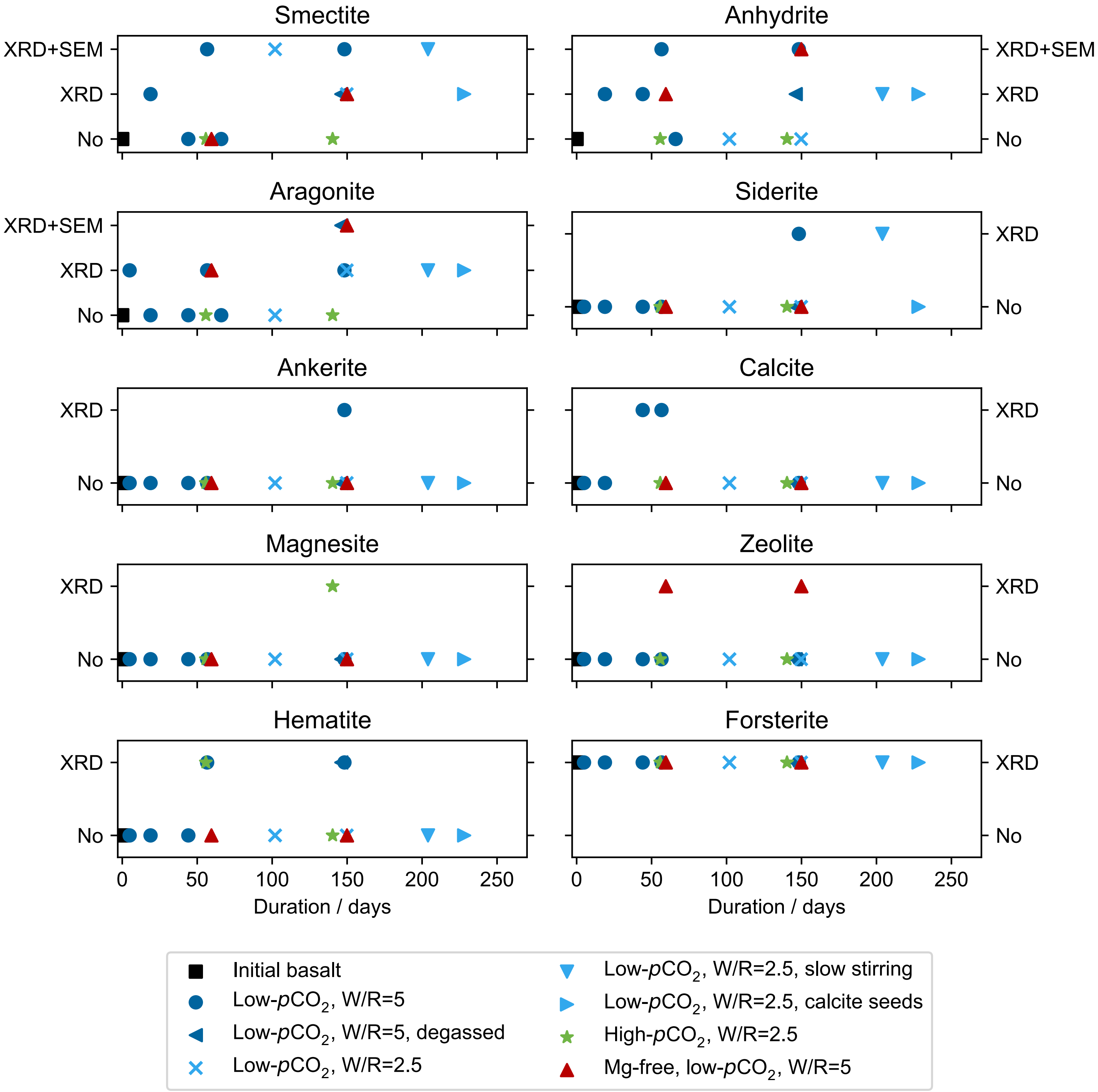
Smectite
Anhydrite
Aragonite
Siderite
Ankerite
Calcite
Magnesite
Zeolite
Hematite
Forsterite
XRD+SEM
XRD
No
0
50
100
150
200
250
Duration / days
■ Initial basalt
● Low-pCO_2, W/R=5
◀ Low-pCO_2, W/R=5, degassed
× Low-pCO_2, W/R=2.5
▼ Low-pCO_2, W/R=2.5, slow stirring
▶ Low-pCO_2, W/R=2.5, calcite seeds
★ High-pCO_2, W/R=2.5
▲ Mg-free, low-pCO_2, W/R=5

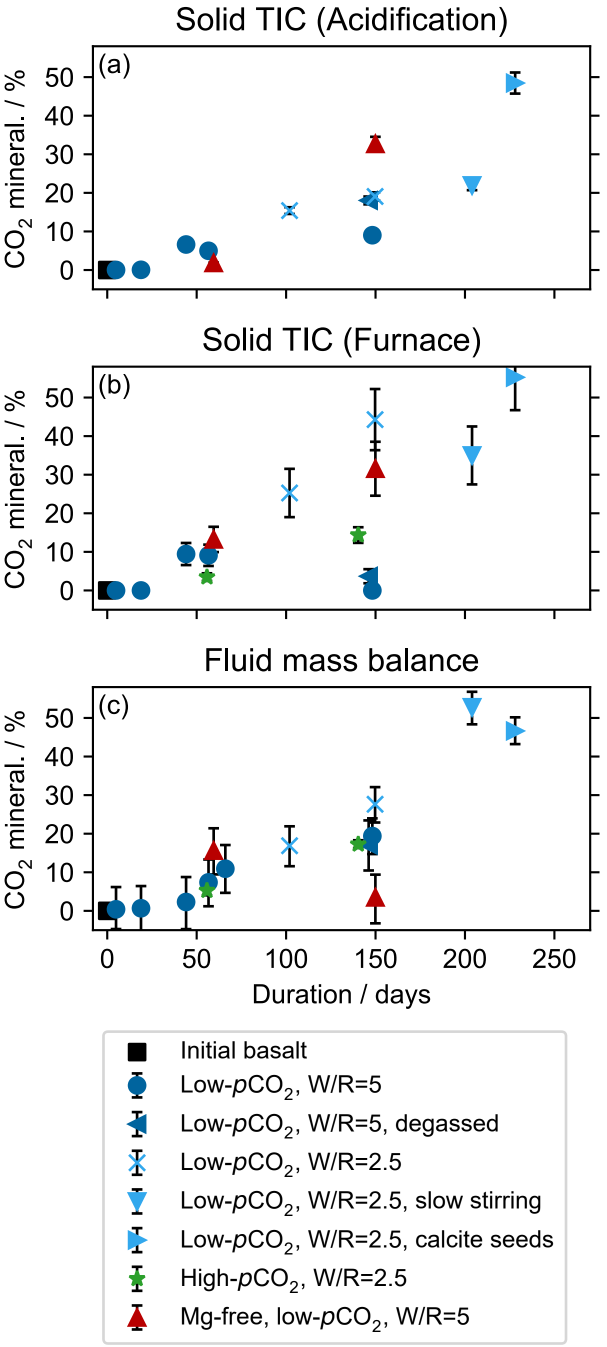
Solid TIC (Acidification)
(a)
Solid TIC (Furnace)
(b)
Fluid mass balance
(c)
CO_2 mineral. / %
0
10
20
30
40
50
Duration / days
0
50
100
150
200
250
Initial basalt
Low-pCO$_2$, W/R=5
Low-pCO$_2$, W/R=5, degassed
Low-pCO$_2$, W/R=2.5
Low-pCO$_2$, W/R=2.5, slow stirring
Low-pCO$_2$, W/R=2.5, calcite seeds
High-pCO$_2$, W/R=2.5
Mg-free, low-pCO$_2$, W/R=5

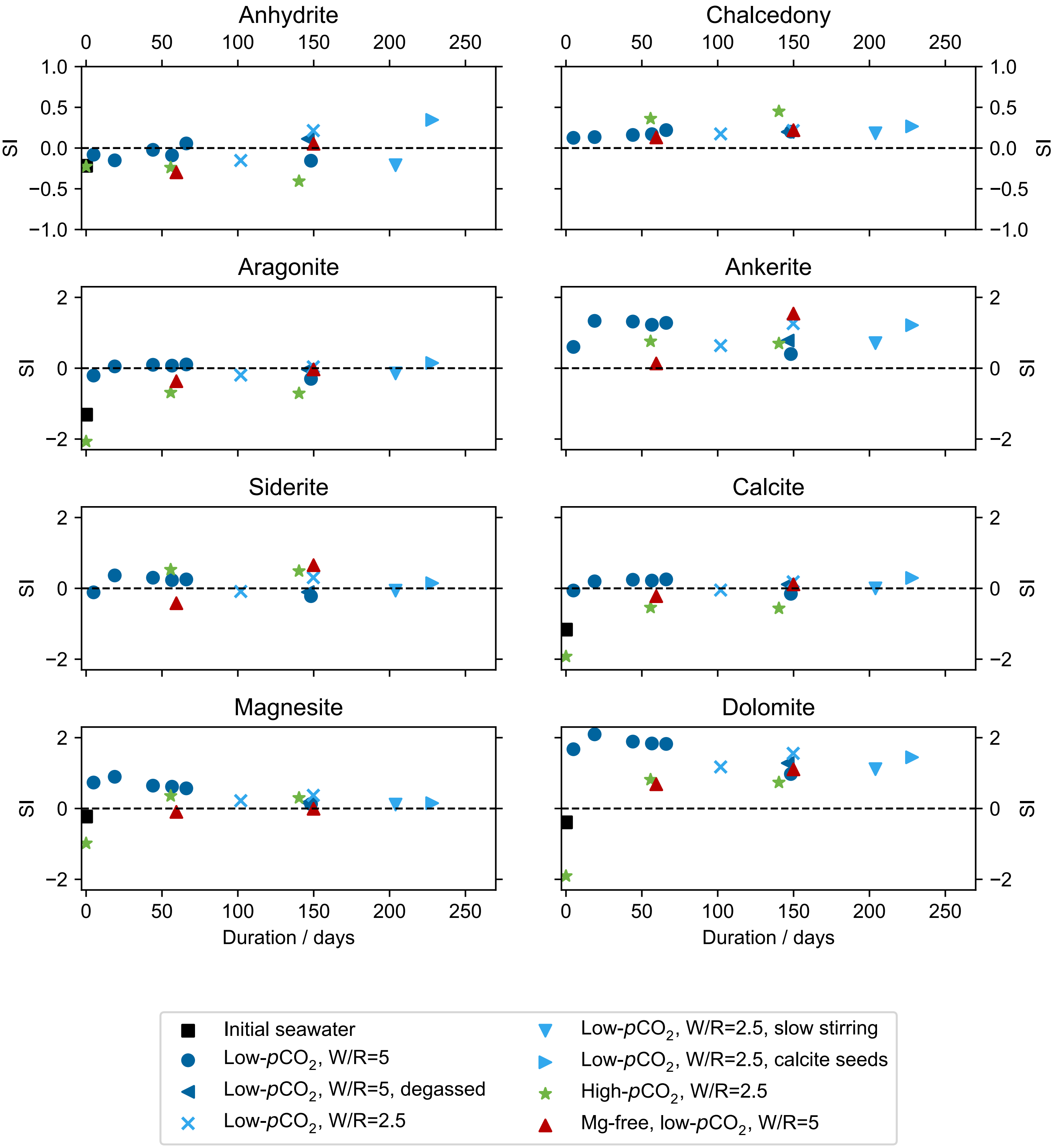
Anhydrite
Chalcedony
Aragonite
Ankerite
Siderite
Calcite
Magnesite
Dolomite
SI
1.0
0.5
0.0
−0.5
−1.0
2
0
−2
0
50
100
150
200
250
Duration / days
Initial seawater
Low-pCO$_2$, W/R=5
Low-pCO$_2$, W/R=5, degassed
Low-pCO$_2$, W/R=2.5
Low-pCO$_2$, W/R=2.5, slow stirring
Low-pCO$_2$, W/R=2.5, calcite seeds
High-pCO$_2$, W/R=2.5
Mg-free, low-pCO$_2$, W/R=5

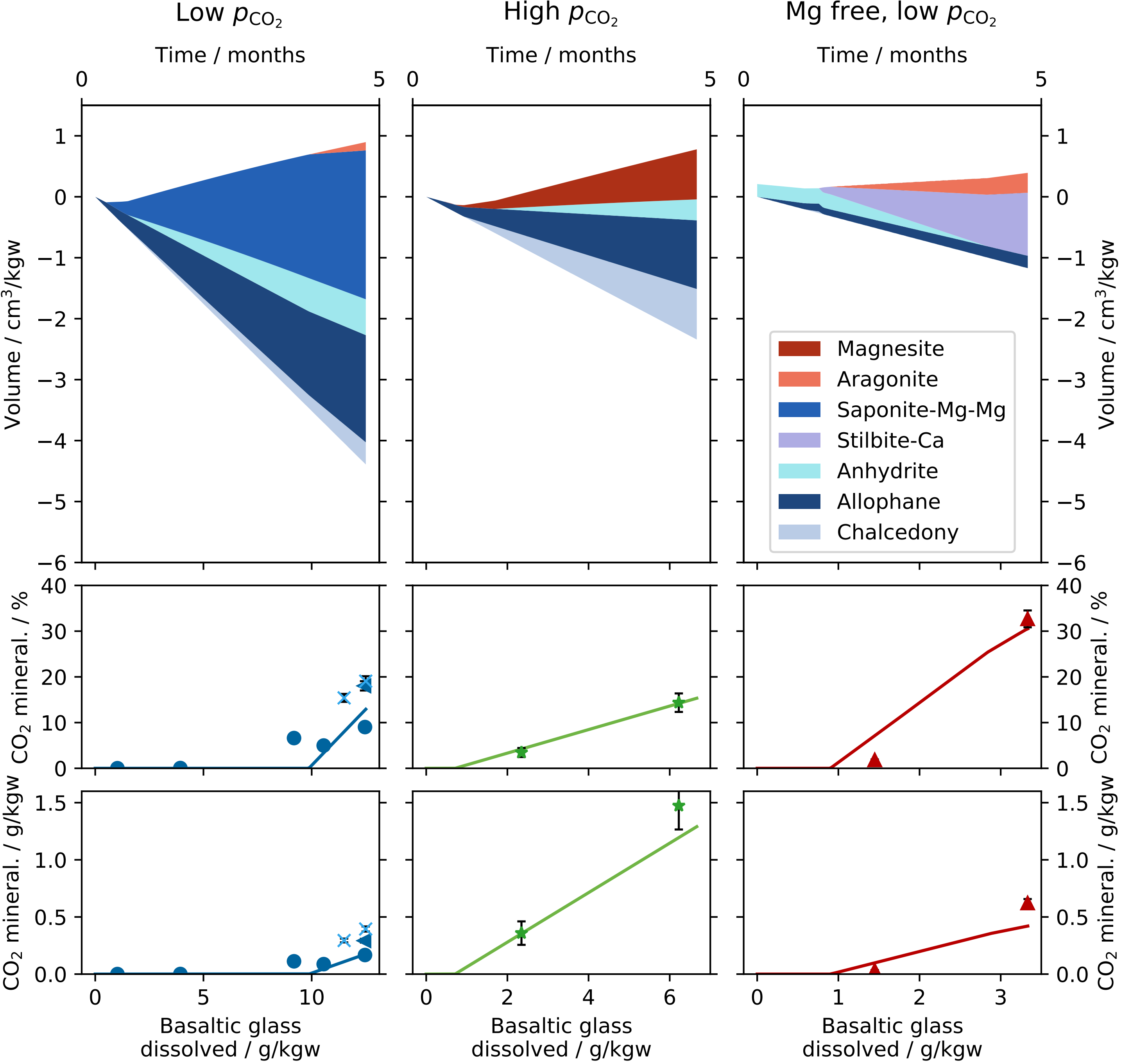
Low p_{CO_2}
High p_{CO_2}
Mg free, low p_{CO_2}
Time / months
0
5
Volume / cm^3/kgw
1
0
−1
−2
−3
−4
−5
−6
Magnesite
Aragonite
Saponite-Mg-Mg
Stilbite-Ca
Anhydrite
Allophane
Chalcedony
CO_2 mineral. / %
0
10
20
30
40
CO_2 mineral. / g/kgw
0.0
0.5
1.0
1.5
Basaltic glass dissolved / g/kgw
0
5
10
0
2
4
6
0
1
2
3

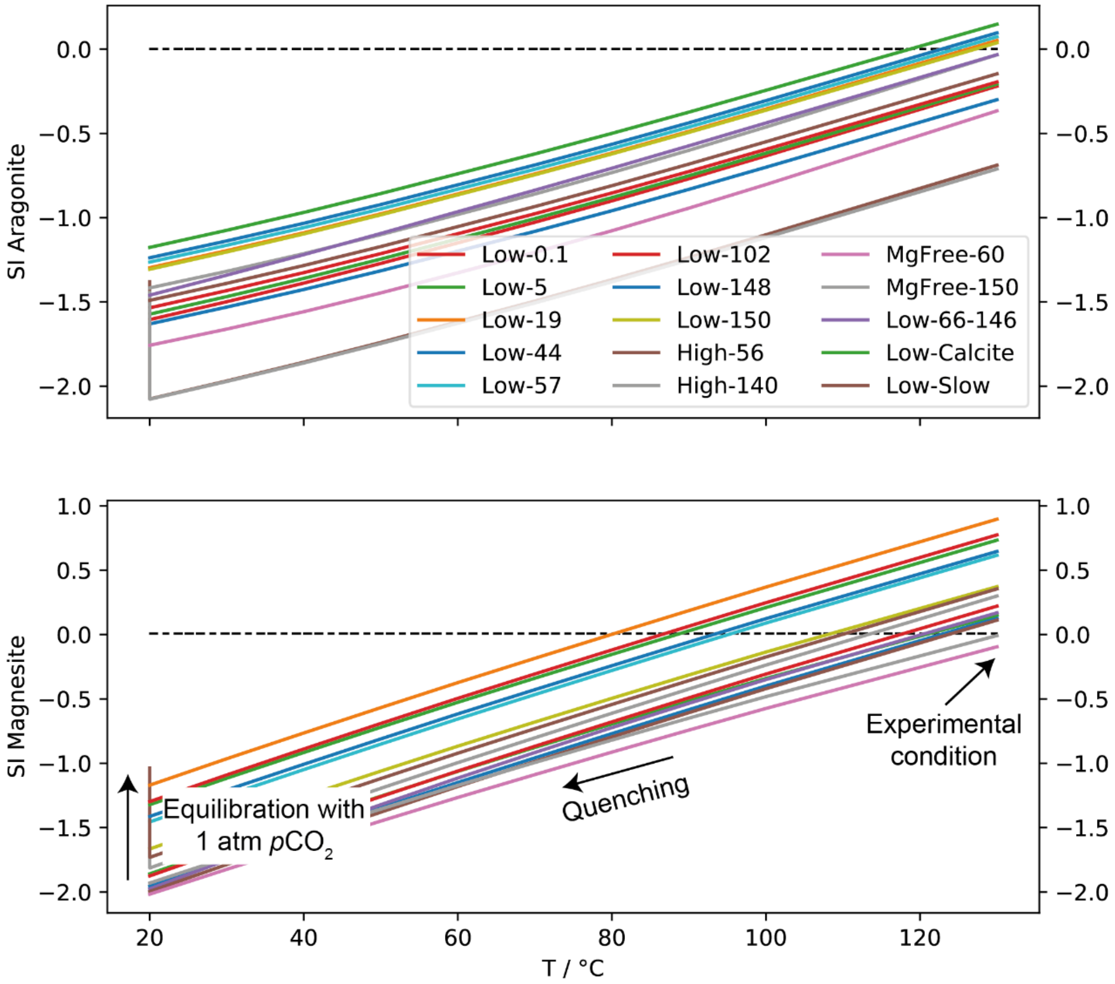

Figure S-1: Saturation indices (SI) of aragonite and magnesite, as predicted by thermodynamic calculations during quenching of the reactors and equilibration to 1 atm pCO_2*.*

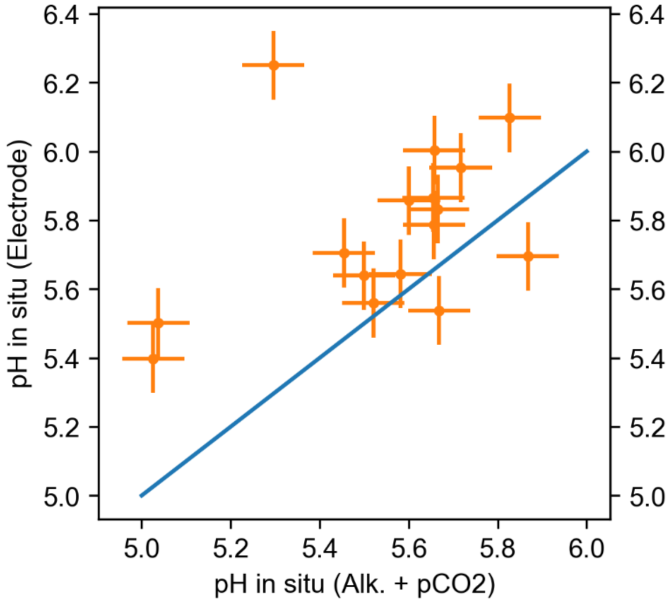

Figure S-2: Comparison between pH calculated for in situ conditions from measured alkalinities, pressure, and fluid composition, versus the pH measured using a pH combination electrode during sampling. Note that degassing of CO_2 *from the solution during sampling likely affected the latter pH measurements, which is consistent with these measurements giving slightly higher pH values in most cases.*

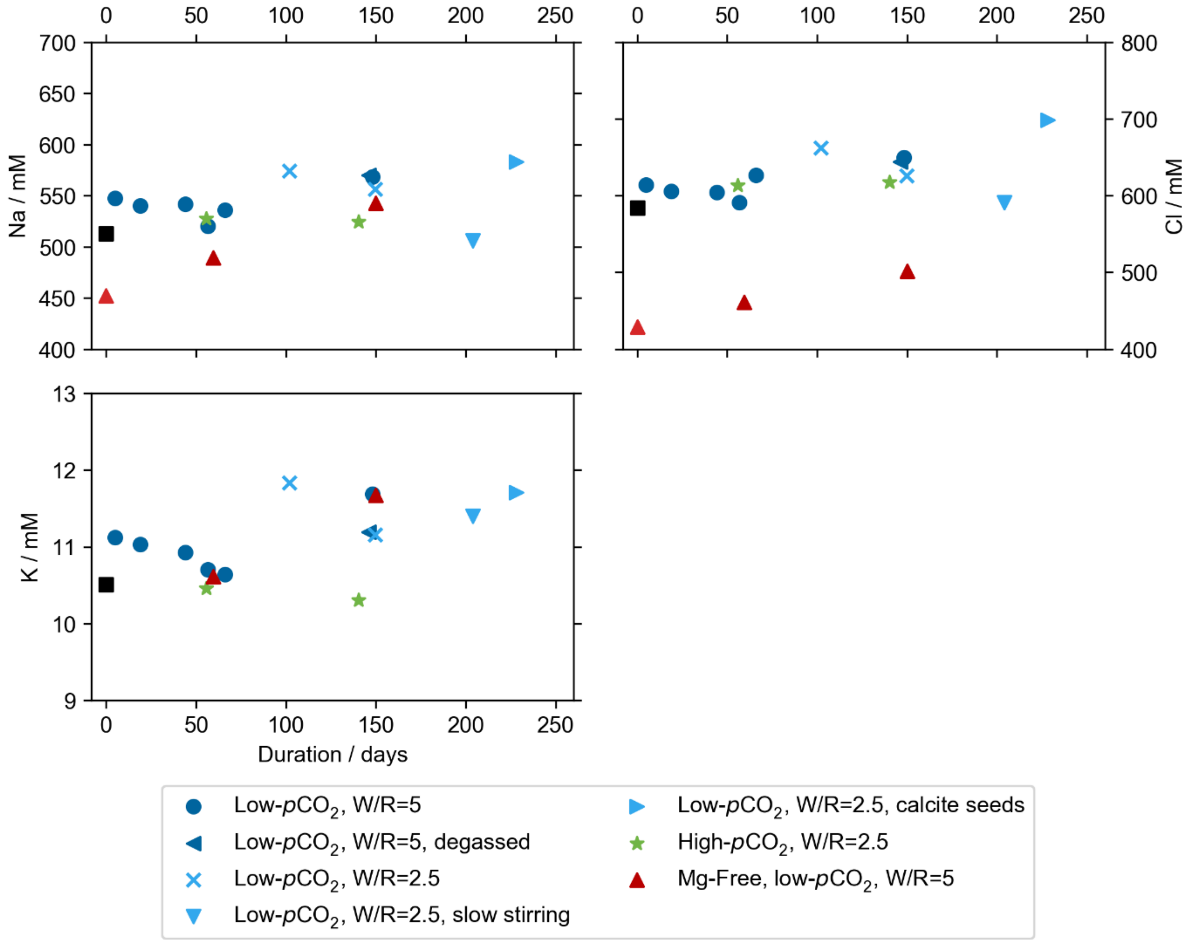

Figure S-3: Plots of measured fluid Na, Cl, and K concentrations of the experiments.

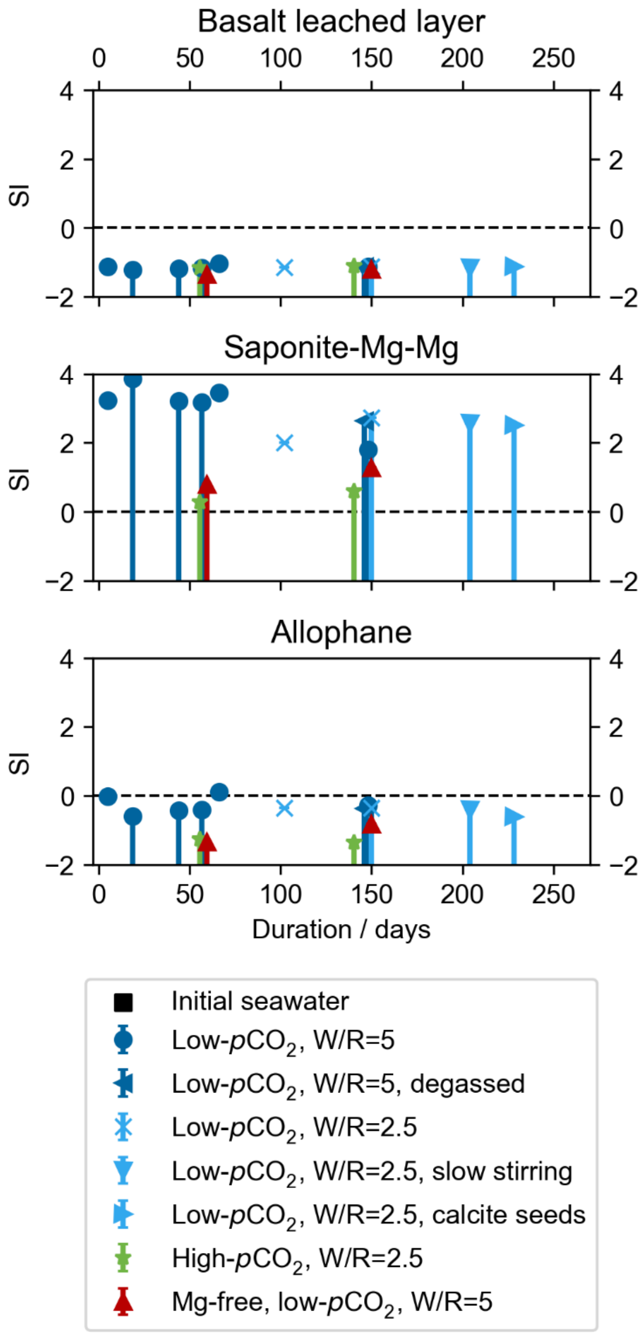

Figure S-4: Diagram showing calculated saturation indices (SI) of the reacted seawater with respect to different alumosilicate minerals. Since aqueous Al concentrations were below the detection limit of ~ 1µM in most cases, SI for those experiments were calculated using 1µM Al and thus represent maximum values, indicated by the error bars below the symbols.

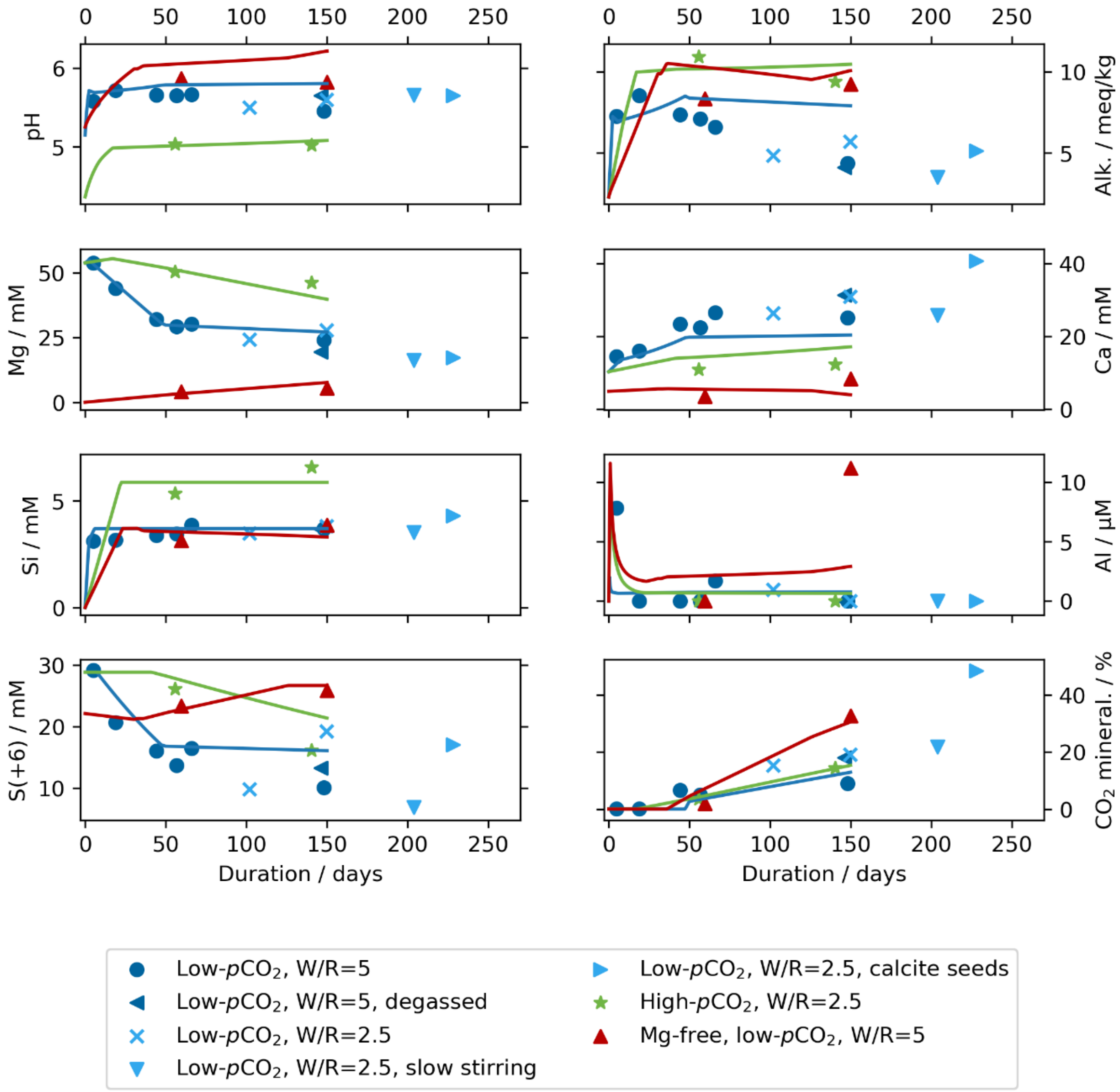

Figure S-5: Plot showing the fit of the reaction path model (solid lines) to the observed fluid composition (points) and CO_2 mineralization (as calculated from measured TIC contents of the solids).

Table S-1: Secondary minerals whose solubility was adjusted during the calibration of the reaction path model and their dissolution reactions. The adjustment is expressed in terms of change of logarithm of the solubility constant log K relative to the values in carbfix.dat.

Mineral	Dissolution reaction	log *K* used
Mg-Mg-Saponite	$Mg_{3.175}Al_{0.35}Si_{3.65}O_{10}(OH)_2 + 7.4\ H^+ = 0.35\ Al^{3+} + 3.175\ Mg^{2+} + 3.65\ SiO_2 + 4.7\ H_2O$	+4
Mg-Fe-Saponite	$Fe_{0.175}Mg_3Al_{0.35}Si_{3.65}O_{10}(OH)_2 + 7.4\ H^+ = 0.175\ Fe^{2+} + 0.35\ Al^{3+} + 3\ Mg^{2+} + 3.65\ SiO_2 + 4.7\ H_2O$	+4
Ca-Stilbite	$CaAl_2Si_7O_{18} \cdot 7\ H_2O + 8\ H^+ =$ $2\ Al^{3+} + Ca^{2+} + 7\ SiO_2 + 11\ H_2O$	+1
Anhydrite	$CaSO_4 = Ca^{2+} + SO_4^{-2}$	-0.1
Aragonite	$CaCO_3 + H^+ = Ca^{2+} + HCO_3^-$	+0.1
Chalcedony	$SiO_2 = SiO_2$	+0.2 +0.4 (high-pCO_2)
Allophane	$Al_2O_3(SiO_2)_{1.22} \cdot 2.5\ H_2O + 2.5\ H_2O =$ $2\ Al(OH)_4^- + 2\ H^+ + 1.22\ SiO_2$	-1 -0.5 (Mg-free)